Numerical modelling of salt diapirism and the temperature field during thin-skinned extension; in search of geothermal and hydrocarbon energy sources

Guido Harms
Utrecht University, department of Earth Sciences

October 30, 2015

Abstract

The occurrence of salt diapirs is strongly associated with potential geothermal and hydrocarbon energy sources. Many numerical modelling studies of diapirism have been done in the past, though very few of these in fact use geologically realistic settings and materials. Besides, only analogue and structural studies have been done on full scale diapirism during thin-skinned extension. Numerical modelling of this problem, using a code called ELEFANT, could answer the following questions: "which parameters affect the growth rate and shape of the diapir, and how?" and "what is the effect of this diapirism on the temperature field and surface heat flux?" The results show that, in compliance with both analogue modelling and structural geological studies, a diapir formed during thin-skinned extension undergoes three phases: reactional piercement, active piercement and passive piercement. Extension rates directly influence the total time required for the diapir to reach the surface, as well as how long the system remains in a state of reactional diapirism, which both affect the shape of the resulting diapir. The mass diffusivity coefficient affects the growth rate of the diapir during its active stage and the total rising time, which affects the shape of the diapir. The density contrast between the salt and the sediments also influences the growth rate during active and passive piercement. Surrounding a rising diapir the temperature is heightened, although not as much as expected. It can, however, still be valuable for hydrocarbon exploration. The heat flux above the diapir is higher than away from the diapir. Besides, both an increased bottom temperature and an increased salt conductivity give higher surface heat fluxes. This makes it an important feature for geothermal energy.

1 Introduction

Due to their properties, salt diapirs are important geological structures with respect to energy resources. Because rock salt is a great conductor of heat compared to normal sedimentary rock types (van Keken et al. 1993), such piercement structures through the sedimentary sequence are expected to greatly affect the temperature field within the host basin. Knowledge of the present-day temperature field, as well as its history, are extremely valuable for possible geothermal energy production or hydrocarbon exploration. When regarding the present day situation, both

heightened temperatures at depth and surface heat fluxes could provide sources for geothermal energy production (Barbier 2002). On the other side, the evolution of the temperature field provides insights for hydrocarbon exploration, in the form of estimated ages and duration of actively producing source rocks (Kauerauf & Hantschel 2009).

Salt diapirs can be found around the globe, and a good many of these are situated in basins that are undergoing thin-skinned extension. Most passive margins have large areas where salt is a major component and where updip the sediment sequence is in extension due to the gravitational sliding caused by the slight incline of the basement. An example of this can be seen at the north Angolan margin (figure 1).

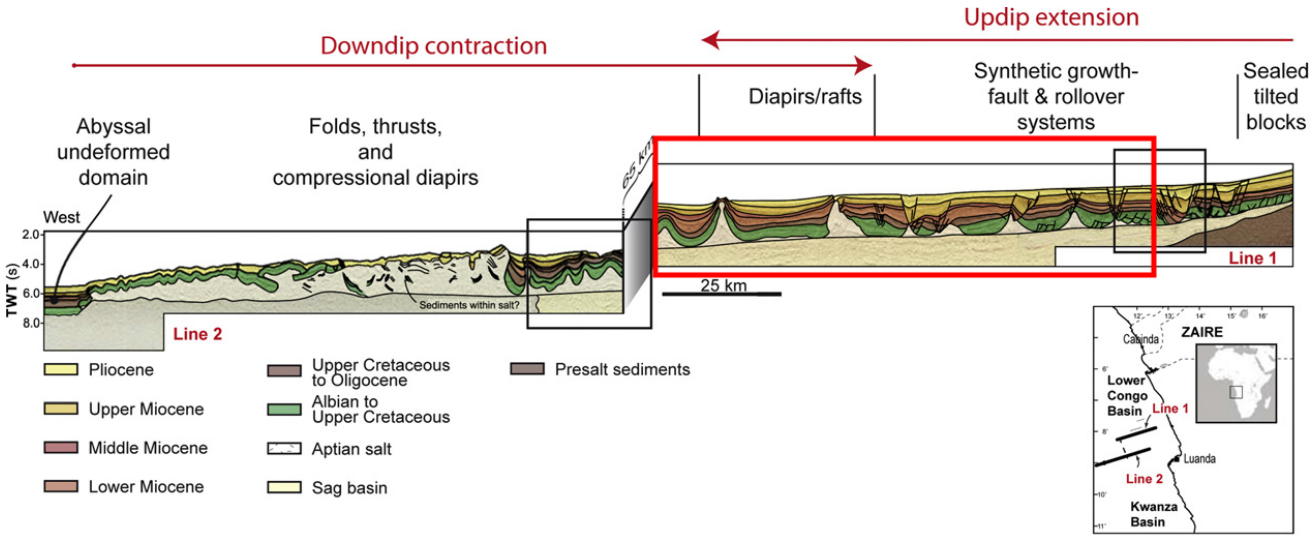

Figure 1: Composite cross section of the north Angolan passive margin. Note the updip extension and diapir formations (red rectangle). Altered from Brun & Fort (2011)

An example of thin-skinned extension above a salt layer which is not located at a passive margin, is in the Canyonlands National Park area in Utah, United States. Here the salt slightly dips towards the Colorado River canyon, where the canyon erosion has provided space for the overlying sedimentary sequence to spread to (figure 2).

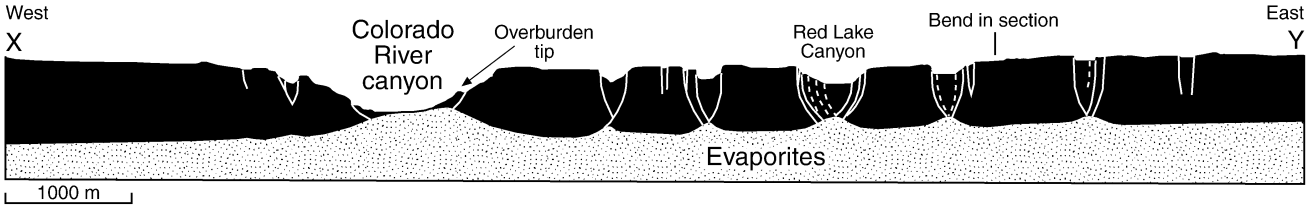

Figure 2: Cross section of the Grabens area of Canyonlands National Park, Utah. From Schultz-Ela & Walsh (2002)

With all of the above in mind, the main aim of this master thesis is to enhance the knowledge of the important factors in both the formation of a salt diapir and the evolution of the associated temperature field, in the case where this diapir forms during thin-skinned extension of the host basin. Basically two questions are addressed:

- which parameters affect the growth rate and shape of the diapir, and how?
and
- what is the effect of this diapirism on the temperature field and surface heat flux?

The research for this work has been successfully conducted using a finite element code called ELEFANT (Thieulot 2014) with a few additions that were implemented for the subject of salt tectonics (Harms 2015). In comparison to conventional analogue modelling, numerical modelling is more flexible in terms of initial setup and boundary conditions and allows for temperature feedback on the rheology. Although numerical modelling studies of diapirism have been done in the past (e.g. Zaleski & Julien (1992); Podladchikov et al. (1993); Poliakov et al. (1993)), very few of these in fact use geologically realistic settings and materials.

In the following chapter a literary overview of the properties of rock salt and the dynamics behind salt diapirism is first provided, followed by a short explanation of ELEFANT and the physics behind it is given. After that, chapter 4 describes the numerical modelling of a diapir, with focus on the structural aspect. In this chapter a reference model without temperature is presented and the effects of a number of parameters are subsequently analysed. In chapter 5 temperature is added to the system and associated parameters are discussed. Finally, a short discussion of the results with respect to the energy resources is presented.

2 Salt tectonics overview

2.1 Salt material properties

Rock salt is defined as a crystalline aggregate of the mineral halite (NaCl). However, salt bodies of a size that is significant in salt tectonics can be assumed to also consist of other evaporitic minerals, as well as small amounts of non-evaporite rocks. Therefore, as in most literature concerning salt tectonics, the term salt or rock salt is used in this work as an overarching concept regarding rock masses that consist for the largest part of halite.

Even under normal crustal conditions, the material properties of salt are quite different from other sedimentary rocks. Compared to normal tectonics, the presence of rock salt layers can lead to differences in deformational styles as well as anomalies in the temperature field.

Halokinesis, or natural salt flow, already occurs at shallow crustal temperatures (i.e. below 150-200^{o}C (Jackson & Talbot 1986)). This flow is accommodated by different types of dislocation creep, possibly accompanied by pressure solution if water is present at grain boundaries (Carter et al. 1993; Spiers et al. 1990). In contrast to the brittle sediments in the upper regions of the crust, halokinesis makes salt behave viscous.

When derived from steady state creep laws, the effective viscosity (μ) of rock salt is shown to depend on temperature and grain size, giving it a range of 10^{16} to 10^{20} Pa.s (van Keken et al. 1993). During this study a mean value of 10^{18} Pa.s is attributed to the salt, partly for computational reasons.

The density (ρ) of a pure single crystal halite mineral is 2170 kg.m^{-3}. However, due to possible contamination of different evaporitic minerals or other impurities, this density will most likely vary in naturally occurring salt layers. Therefore we adjust the salt density in this study to a rounded value of 2100 kg.m^{-3}. Salt is also rather incompressible compared to other sedimentary rocks (i.e. carbonates and siliciclastics), which might lead to even larger differences in density at

greater depths.

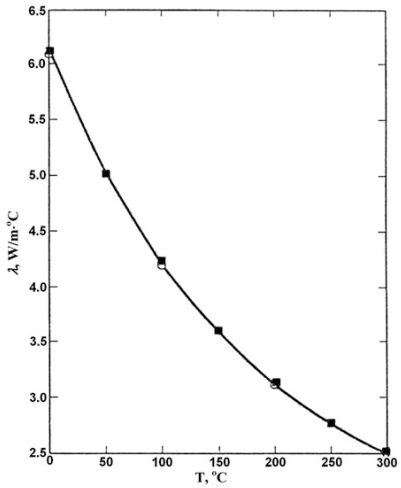

Figure 3: Experimental data on conductivity of rock salt as a function of temperature. From Blesh et al. (1983)

The thermal conductivity of salt has been shown to depend greatly on temperature, especially in the temperature ranges seen in the upper crust (0-200^{o}C) (see figure 3), where it can value from around 3 W.m^{-1}K^{-1} up to 6.1 W.m^{-1}.K^{-1}. Furthermore, the heat capacity at constant pressure (c_p) of rock salt is 518 J.kg^{-1}.K^{-1} (Blesh et al. 1983).

2.2 Salt flow

As explained above, salt is mechanically weak and can flow like a fluid when regarded on tectonic time scales.

2.2.1 Driving Salt flow

It is now recognized that although salt bodies are overall less dense than their overburden, the resulting buoyancy forces are not the main drive behind salt flow. This is mainly due to the fact that the overburden consists of rigid, brittle rocks, instead of just another fluid with a different viscosity and density, as had been assumed in the majority of studies in the previous century (e.g. Zaleski & Julien (1992); Podladchikov et al. (1993); Poliakov et al. (1993)).

Instead, salt flow is assumed to be dominantly driven by differential loading, while the opposing forces are the strength of the overburden and boundary friction within the salt layer (Hudec & Jackson 2007). When the driving forces overcome these resisting forces the salt will flow, otherwise it can remain at rest for significant amounts of time. Differential loading with respect to salt tectonics is often divided into three types: gravitational loading, displacement loading and thermal loading. All of these can occur simultaneously, although it depends on the geometry of the salt body, pressure and temperature conditions and geological setting which mechanism is most important.

Gravitational loading is caused by both the weight of the overburden and the gravitational body forces in the salt body itself. Simplifying, this mechanism can be compared to the concept of hydraulic head in fluid statics, which is illustrated in figure 4 (Hudec & Jackson 2007).

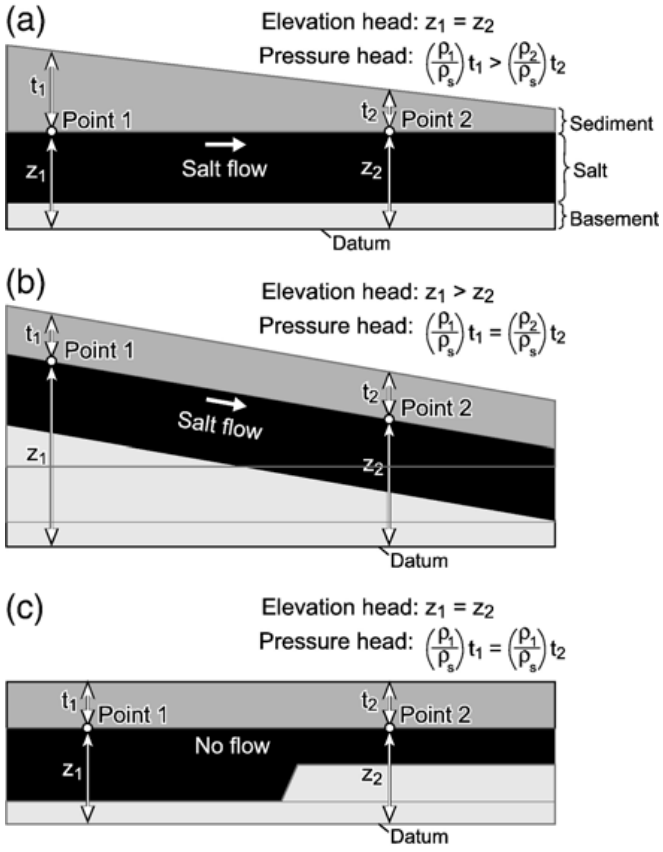

Figure 4: Examples of hydraulic head-gradient analysis in salt tectonics. a): for a laterally varying overburden thickness. b): above an inclined surface. c:) with varying salt thickness but no varying overburden thickness. From Hudec & Jackson (2007).

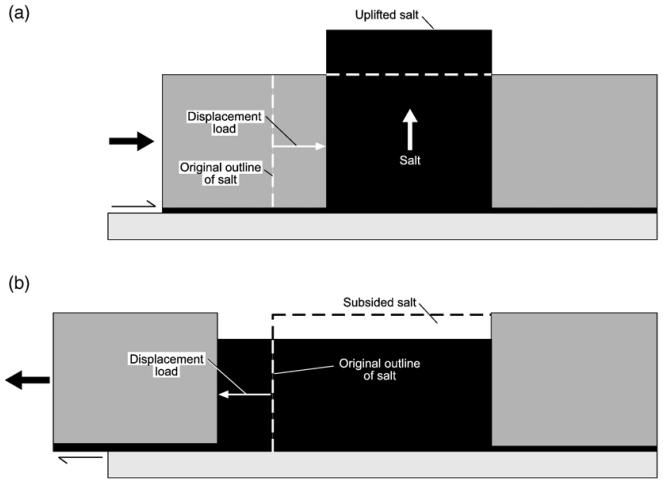

Figure 5: Schematic visualization of displacement loading on pre-existing salt structures. a): during shortening and b): during extension. From Hudec & Jackson (2007).

Displacement loading is the effect created by externally forcing relative displacement of one boundary of a rock body to another (figure 5).

Thermal loading results from temperature induced volume changes, affecting the buoyancy of (parts of) a salt body. It is proposed that this can even cause intrasalt convection (Talbot 1978;1982).

2.2.2 Resisting salt flow

Above described driving forces are assumed to be present at all times in nature. However, there are still salt bodies which remain static. This is due to two factors that resist the flow of salt.

Firstly there is the overburden, which, if strong enough, can resist any deformation the movement of salt would cause. This leaves no space for the salt to flow to and thus inhibits any flow at all.

The second factor that limits flow is boundary drag at the top and bottom interfaces of the salt and surrounding rocks. Depending on the thickness of the salt layer as well as the flow law that governs the flow (either Newtonian or power-law viscous), the viscous shear forces generated at the interfaces may also effectively immobilize the salt.

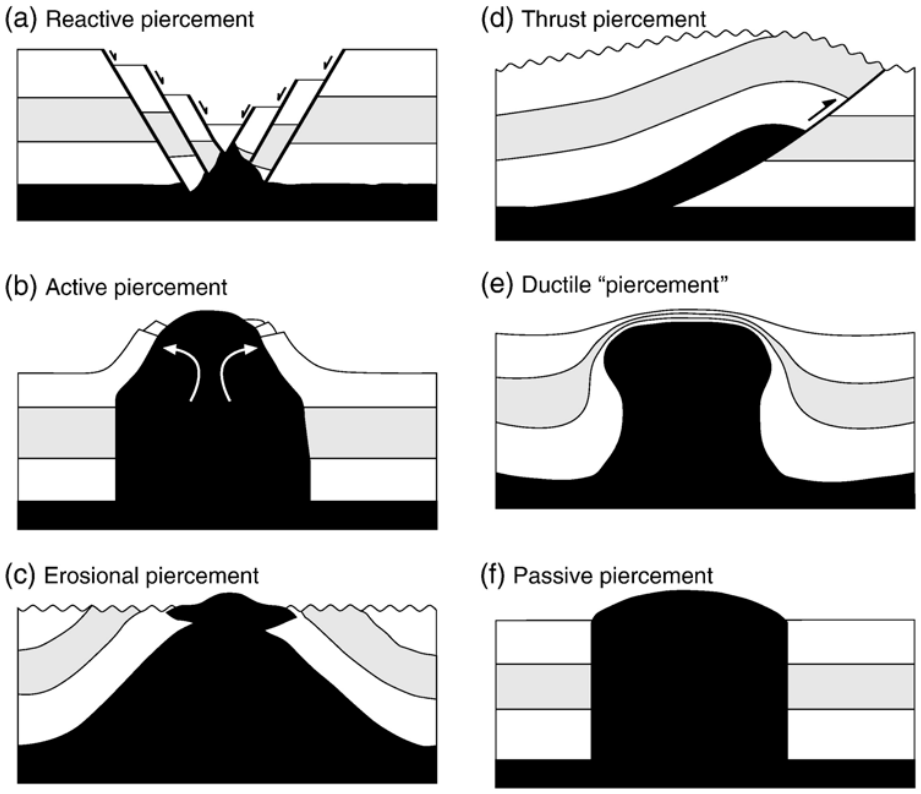

Figure 6: Schematic overview of different modes of diapirims. From Hudec & Jackson (2007).

2.3 Diapirism

The most distinct feature seen in salt tectonics is the formation of salt diapirs. In order for the salt to be able to pierce upward through the overlying sequence and form a diapir, room must be created by either removing or displacing the rocks occupying that space. When dealing with brittle overburdens this can happen in four ways.

Firstly, extension in the overburden causes it to break into different fault blocks, which can be separated to accommodate the reactively piercing salt (figure 6a). Secondly, a diapir may actively and forcibly lift, rotate and shoulder aside flaps of overburden (figure 6b). Thirdly, erosion can remove part of the roof (figure 6c). Finally, the salt may be accommodated in the hanging wall of a thrust fault (figure 6d).

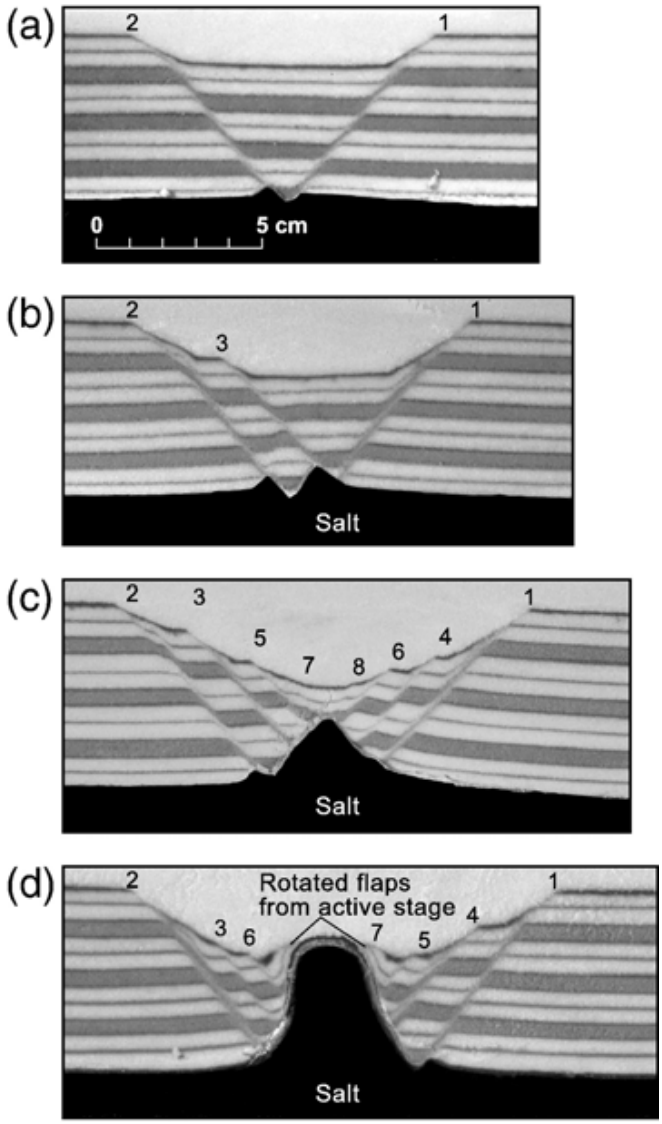

Figure 7: Results of an analogue experiment on diapirism during thin-skinned extension, showing stages of a,b and c): reactive piercement and d): active piercement. From Vendeville & Jackson (1992).

Diapirs that have to deal with "fluid" overburdens (e.g. soft sediments) can pierce upward

due to ductile thinning of the roof (figure 6e). These types of overburdens are quite rare and strictly speaking the resulting salt bodies are not actual diapirs because they are not in discordant contact with the surrounding materials. However, they have risen with respect to the flanking sequence and are often shaped like diapirs in the classical sense (i.e. plumelike).

A sixth type of diapir growth becomes possible when the overburden has been completely pierced and the diapir is exposed at the surface. Here it continues rising relative to the surrounding strata while remaining exposed and new sediments are accumulated around it. This mode is known as passive diapirism or downbuilding (figure 6f).

Salt diapirism has been the subject of many studies, from analogue experiments (e.g. Vendeville & Jackson (1992); Nalpas & Brun (1993)) to numerical modelling (e.g. Zaleski & Julien (1992); Petersen & Lerche (1994); Nikolinakou et al. (2013); Massimi et al. (2007); Fuchs et al. (2015)) and purely structural geological (e.g. Harding & Huuse (2015); Hudec & Jackson (2007); Brun & Fort (2011)). However, as mentioned before, only analogue and structural studies have been done on full scale diapirism as a result of thin-skinned extension. Therefore, for later comparison, the results from one analogue experiment are presented in figure 7.

3 Physics and numerics

As mentioned before, the aim of this study is to determine the important factors and their effects in the formation and temperature evolution of a salt diapir formed during thin-skinned extension. This was done by numerical modelling of such a tectonic event. The following section explains the physics behind the models and the code that is used.

3.1 Physics

When we assume that materials in the Earth's crust behave like incompressible, visco-plastic fluids, they are required to obey the following form of the Stokes equations:

$$\nabla(\mu\boldsymbol{\nabla}\boldsymbol{v}) - \boldsymbol{\nabla}p + \rho\boldsymbol{g} = \mathbf{0} \tag{1}$$

and

$$\boldsymbol{\nabla}\cdot\boldsymbol{v} = 0 \tag{2}$$

These are derived from the following closed set of equations:

$$\boldsymbol{\nabla}\cdot\boldsymbol{\sigma} + \rho\boldsymbol{g} = \mathbf{0} \tag{3}$$

$$\boldsymbol{\sigma} = -p\mathbf{1} + \boldsymbol{s} \tag{4}$$

$$\boldsymbol{s} = 2\mu\dot{\boldsymbol{\epsilon}} \tag{5}$$

$$\dot{\boldsymbol{\epsilon}} = \frac{1}{2}(\boldsymbol{\nabla}\boldsymbol{v} + (\boldsymbol{\nabla}\boldsymbol{v})^T) \tag{6}$$

Equation (2) is the mass conservation equation for incompressible fluids, where $\boldsymbol{v}$ is the velocity field. Equation (3) is the momentum conservation equation in which ρ is the mass density, g is the gravitational acceleration and σ is the Cauchy stress tensor. The latter is described in equation (4), where it is divided into a spherical part $-p\mathbf{1}$ and its stress deviation $\boldsymbol{s}$, which is in turn described in equation (5). Here, μ is the dynamic viscosity and $\dot{\boldsymbol{\epsilon}}$ is the strain rate tensor. Finally, $\dot{\boldsymbol{\epsilon}}$ can be related to the velocity field $\boldsymbol{v}$ using equation (6).

Although we are dealing with shallow crustal levels and relatively low temperatures, certain material properties (e.g. density and viscosity) do depend on the latter, making it therefore necessary to compute the temperature field. This is done by solving the heat transport equation:

$$\rho c_p \left(\frac{\partial T}{\partial t} + \boldsymbol{v} \cdot \boldsymbol{\nabla} T \right) = \boldsymbol{\nabla} \cdot (k \boldsymbol{\nabla} T) + H_r + H_s \tag{7}$$

where T is the absolute temperature, c_p is the heat capacity, k is the thermal conductivity, H_r is the internal heat production from radioactive decay and H_s is the heat production due to dissipative or shear heating, which is given by $H_s = \boldsymbol{\sigma} : \dot{\boldsymbol{\epsilon}}$ (Schott et al. 2000; Hartz & Podladchikov 2008; Thielmann & Kaus 2012). As mentioned above, the thermal conductivity can vary with temperature. However, to avoid non-linearity in the temperature equation, each rock type will be given a constant (i.e. not temperature dependent) value for each of above material 'constants'.
The mass density ρ in turn depends on temperature following:

$$\rho(T) = \rho_0 (1 - \alpha (T - T_0)) \tag{8}$$

where α is the coefficient of thermal expansion and ρ_0 is the density at $T = T_0$.

3.2 Rheology and Material memory

At low temperatures, strain in the rocks is accommodated by faults systems. In continuum mechanics such brittle behaviour can be approximated by localized viscous deformation following a plasticity criterion (Kachanov 2004). To limit deformation generated stresses, values of the viscosity are locally adapted. The yield function F applied here is described as follows:

$$F = \sqrt{J_2'} - \sigma_p(p, \dot{\epsilon}, \epsilon) = 2\mu\sqrt{E_2'} - \sigma_p(p, \dot{\epsilon}, \epsilon) \tag{9}$$

Here, J_2' is the second invariant of the deviatoric stress and σ_p is the yield value, which can depend on the pressure field, strain rate and accumulated strain. In case $F > 0$, brittle behaviour ensues and in order to keep the nonlinear relationship between strain rate and stress, the viscosity is rescaled to

$$\mu_{eff} = \frac{\sigma_p(p, \dot{\epsilon}, \epsilon)}{2\sqrt{E_2'}} \tag{10}$$

At higher temperatures materials start behaving fully viscous, using a blend of diffusion and dislocation creep mechanisms. In this regime the effective viscosity is given by a general power law:

$$\mu_{eff} = \frac{1}{2} \left(\frac{d^p}{A C_{OH}^r} \right)^{\frac{1}{n}} {E_2'}^{\frac{1-n}{2n}} \exp\left(\frac{Q + pV}{nRT} \right) \tag{11}$$

where d is the grain size, p the grain size exponent, A is a material constant, C_{OH} the water content, r the water content exponent, n the power law stress exponent, E_2', as before, is the second invariant of the deviatoric strain tensor $\dot{\epsilon}$, Q the activation energy, V the activation volume, R the molar gas constant and T the temperature. For diffusion creep $p > 0$ and $n = 1$ while for dislocation creep $p = 0$ and $n > 1$. In the models described in this study, none of the rocks reach this viscous stage, as temperatures remain too low, except for the salt which is linear viscous from the start.

When deformation progresses, more and more strain is accumulated. When this strain reaches a threshold value, the materials start to strain-weaken until they reach a second threshold value, where the rocks have reached their weakest state. It is assumed that both cohesion c and angle of friction ϕ decrease linearly with strain ϵ. In case of the latter: if ϵ is less than a threshold value ϵ_1, then $\phi = \phi_0$. When $\epsilon_1 < \epsilon < \epsilon_2$, $\phi(\epsilon)$ is defined as follows:

$$\phi = \phi_0 + (\phi_\infty - \phi_0)\frac{\epsilon - \epsilon_1}{\epsilon_2 - \epsilon_1} \tag{12}$$

Lastly, when $\epsilon \geq \epsilon_2$, ϕ is set to ϕ_∞ (or ϕ^{sw}) and remains constant. The same applies for the cohesion.

3.3 Numerical implementation

Above described physics are solved using a finite element code called ELEFANT (Thieulot 2014), which iteratively solves for the velocity and pressure fields. The code makes use of an Arbitrary Langrangian-Eulerian (ALE) grid, which allows for a true free surface (Thieulot 2011; 2014). Material tracking is done using a Marker-in-Cell technique, where Langrangian material markers are advected with a velocity obtained by interpolating the velocity field. The number density of markers is variable and dynamically adapted.

A simple surface processes algorithm has been implemented, which uses a one dimensional diffusion equation (Harms 2015):

$$\frac{\partial h}{\partial t} = k_{sp}\nabla^2 h \tag{13}$$

where k_{sp} is the mass diffusivity coefficient and h is the elevation. This equation is a first order approximation of combined hill-slope processes and deposition in the valley. However, it does not take into account longer range mass transport by for example rivers (Kittenrød 2011). Note that the mass diffusivity coefficient k_{sp} can depend on spatial position (x, h) (e.g. asymmetric weathering) and the slope of the hill-slope $\frac{\partial h}{\partial x}$, or $k_{sp}(x, h, \partial h/\partial x)$.

ELEFANT was created mainly for the modelling of larger scale mantle or full lithosphere processes. The resolution of such models is overall lower than the resolution of the models in this work. This posed a problem when solving for the temperature field. The size of each tectonic time step, which is also used in the heat transport equation (equation (7)), is made to comply with the Courant-Friedrichs-Lewy condition (Anderson 1995; Thieulot 2014):

$$dt = Cmin\left(\frac{h}{|v|_\infty}, \frac{h^2}{\kappa}\right) \tag{14}$$

where C is the Courant number chosen in [0,1], h is a measure of the smallest element size, and κ is the thermal diffusivity given by $\kappa = k/\rho c_p$. In the case of the high resolution models in

this work, the temperature diffusion part dominates the Courant-Friedrichs-Lewy condition. The resulting time step size, however, is multiple orders of magnitude smaller than it could be for the tectonic processes. This means that for the models to fully evolve, many more time steps are required, which makes running these models very time consuming. Therefore, to speed up the runtime, a separate time stepping loop is implemented for solving for the temperature field, very similar to the one for solving the surface processes diffusion equation. This heat transportation time step dt_T now complies to the temperature diffusion part of the Courant-Friedrichs-Lewy ($dt_T = C\frac{h}{|v|_\infty}$), whereas the tectonic time step is only affected by the velocity part ($dt_{tect} = C\frac{h^2}{\kappa}$). The heat transportation algorithm is now ran until

$$\sum dt_{T,i} = dt_{tect}$$

where i is the number of heat transportation time steps.

It should be noted that although ELEFANT is able to deal with three dimensional models, time and other resources dictate that we remain in 2D.

4 Modelling diapirism

Before the temperature field evolution around a diapir formed during thin-skinned extension can be assessed, it is important to determine what factors affect the shape and growth rate of the resulting salt body. Therefore, a reference model, in which temperature is neglected, is created in the first place. In the subsequent runs certain parameters in this reference model will be changed separately and their effects on the evolution of the diapir growth are assessed and discussed. The reference model is a product of an extensive and time consuming search for a combination of material properties and boundary values, of which the results best fit the results of the analogue experiment shown in figure 7. Note that while each parameter is assessed separately, a whole spectrum of combinations of parameter values is of course possible in nature.

Besides being two dimensional, the overall setup of the models in this research has a few other limitations. For instance, as in all finite element codes, mass conservation does not allow pure sedimentation (i.e. without local erosion), nor the compaction of rocks. Elasticity is also not yet implemented in the version of the code that was used, so that folding of rock layers does not occur. However, in this type of diapirism this is not a major issue. Also, the lack of a slightly inclined basement surface somewhat limits the comparison to naturally occurring situations as described in the introduction.

All models/runs described in this work can be found in appendix A. In each following subsection, the setup of the associated run is provided, followed by a description of the results and finally a discussion of these observations.

4.1 Reference model

The reference model has a domain of 20 x 4 km, with 500 x 100 = 50,000 elements giving a resolution of 40 x 40 m. The bottom 1.5 km consists of rock salt with a linear viscous rheology, with density $\rho_0 = 2100$ kg.m^3, viscosity $\mu = 1$ x 10^{18} Pa.s. Above that is a multi layer sequence of 2 types of sedimentary rocks, a total of 2.5 km thick. Both have nonlinear plastic rheology. Rock type 1 has $\rho_0 = 2500$kg.m^3, $\mu_0 \approx 1$ x 10^{24}Pa.s, cohesion $c = 55$ MPa (max strain weakened

to 17.5MPa) and angle of friction $\phi = 32^o$ (max s.w. to 27^o). Rock type 2 has $\rho_0 = 2400$kg.m^3, $\mu_0 \approx 1$ x 10^{24}Pa.s, cohesion $c = 62$ MPa (max s.w. to 25 MPa) and angle of friction $\phi = 3^o$ (max s.w. to 25^o). In the center of the domain at 2 km depth a weak seed of strain weakened material (250x250 m) is located to control the location of initial deformation and preventing the system to deform in an unrealistic pure shear form. The top boundary is free surface and the bottom boundary condition is free slip. The domain is put under extension by prescribing a horizontal velocity of u= - 0.1 cm.year^{-1} on the left boundary and u= + 0.1 cm.year^{-1} on the right boundary, making it a combined extension rate of 0.2 cm.year^{-1} (figure 8). The diffusivity coefficient from surface processes equation (13) is set to $k_{sp} = 10^{-8}$ m^2.s^{-1}.

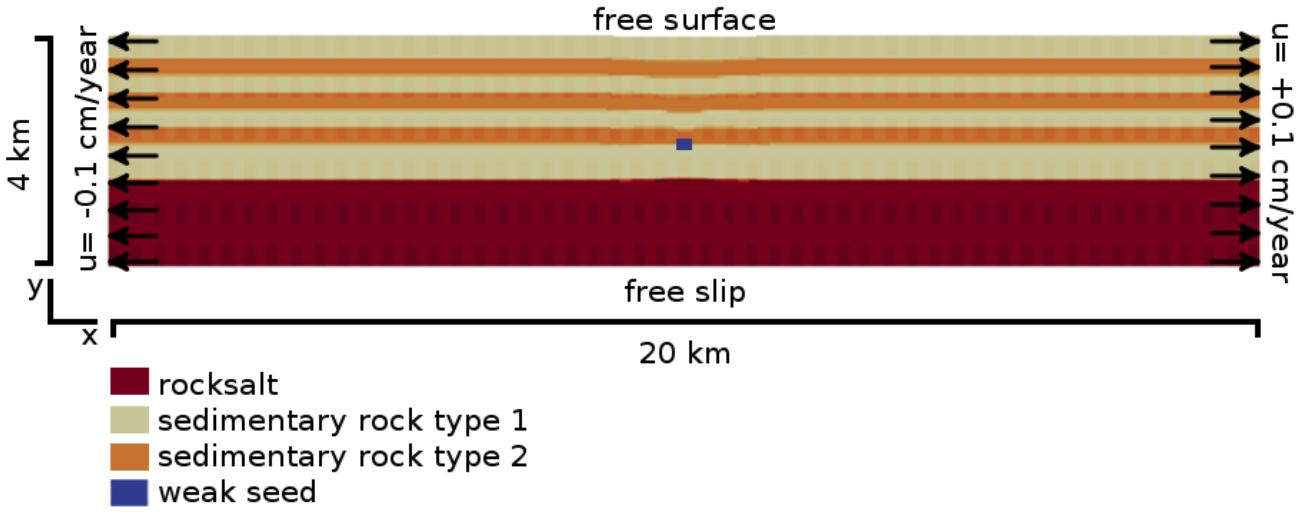

Figure 8: Reference model set up.

Figure 9 shows the time evolution of the reference model. The resemblance of these results to the analogue modelling results shown in figure 7 is striking, albeit not completely similar.

The same stages of diapirism as in before mentioned analogue model can be observed in our results. Figure 9a to d show the "sinking" wedge and the slight uplifting of the basin shoulders combined with the formation of initially one reactive diapir. After 350 kyr the wedge point reaches the salt and starts dividing the diapir in to two. At around 800 kyr some slight numerical asymmetry has caused the left diapir to become slightly larger than the one on the right. Also, the overburden above the left diapir has decreased enough that this diapir enters its active stage. As seen in figures 9f and g, it now actively pushes a small block of sediments upwards as well as causing some rotation and upwards movement of the wedge. Finally at around 1 Myr the diapir has reached the surface of the graben and continues to grow passively (figure 9h).

The final shape of the diapir in the reference model is also quite similar to the one in the analogue model: a base that is only slightly wider than the middle part and a rather rounded head. The only major differences are that it is not located in the center of the graben and that it is slightly more askew. The latter is a result of the shape of the wedge (which remains mostly the same over time) and the angle of the fault.

The greatest difference with respect to the analogue model is that in this model no further faulting (see figure 7b,c) appears necessary to create accommodation space for the salt. To try

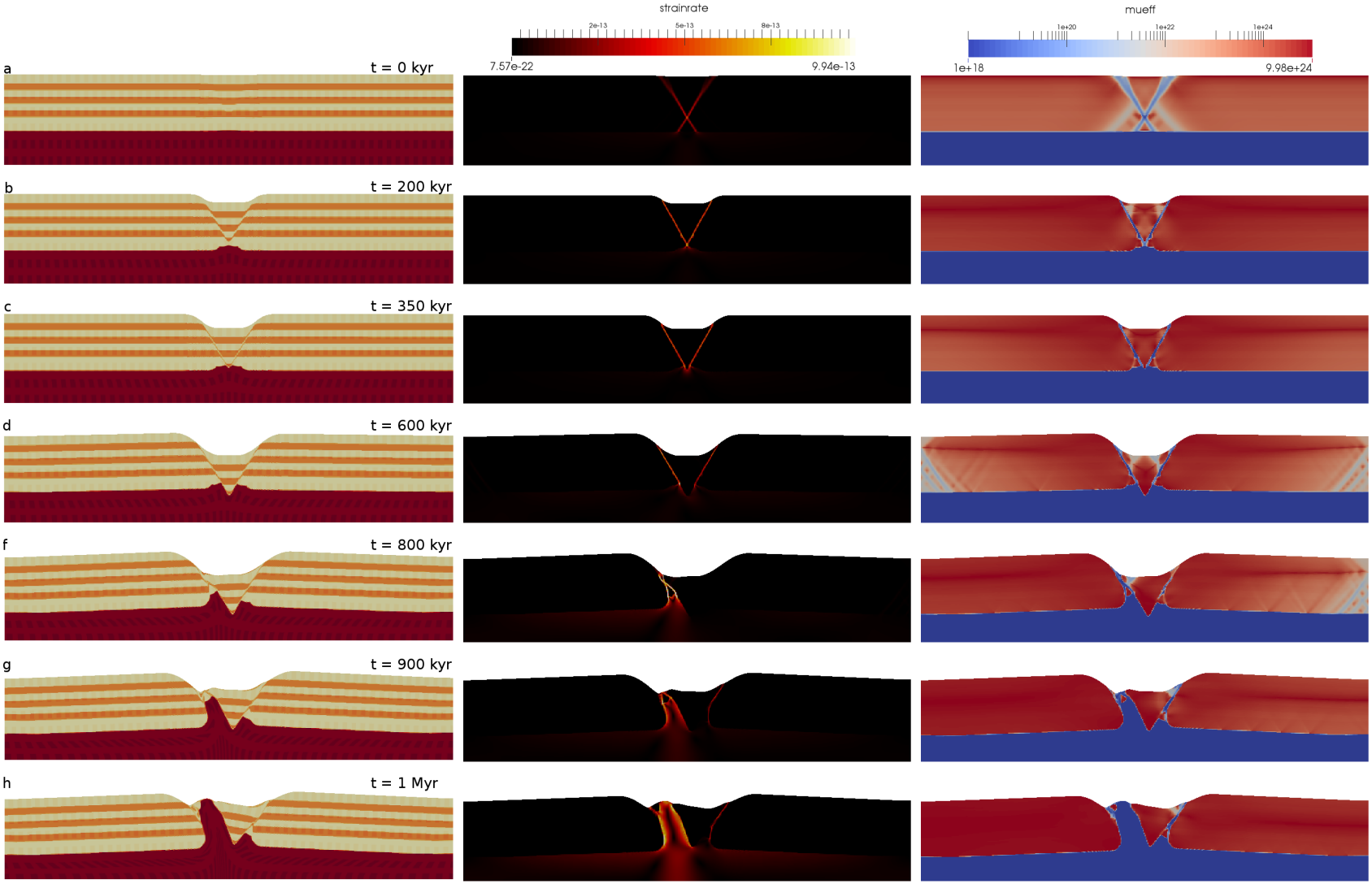

Figure 9: Evolution of the reference model. Left column): materials; middle column): strainrate field; right column): effective viscosity.

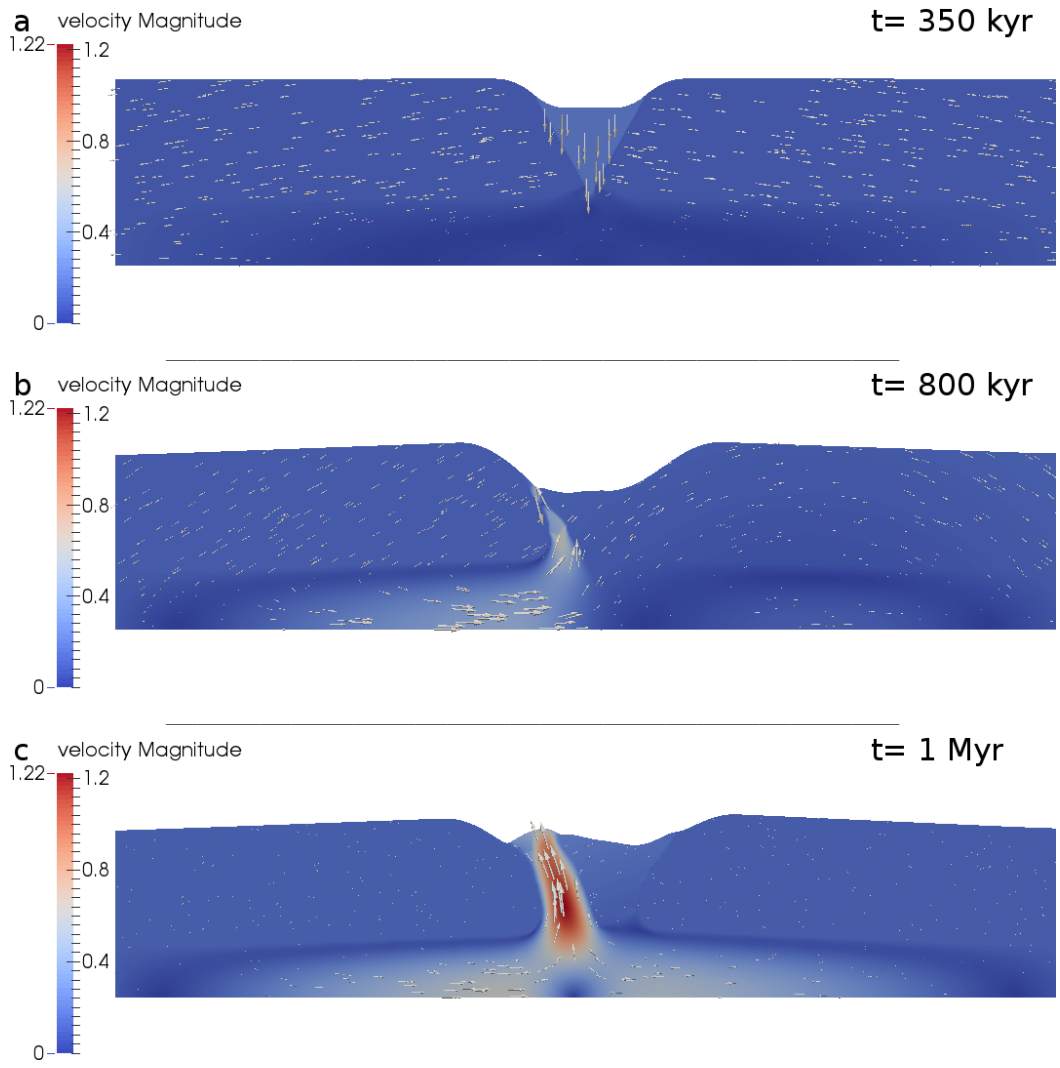

Figure 10: Reference model velocity fields for three different stages: a): during reactive stage; b): during active piercement and c): after full piercement has been achieved. Velocities are in cm.year^{-1}.

and acquire results more similar to the ones of figure 7, further experiments have been done. In these, extra weaknesses in the form of fault shaped strain weakened zones were added to the pre-wedge. However, these tests did not lead to significantly different results and are therefore not shown in this work.

Figure 10 shows the velocity fields during the three stages of diapirism. During the reactive part the salt moves at very slow rates, limited by the rate of formation of accommodation space (figure 10a). Although the extension rate is geologically quite fast, it is mostly accommodated by the sinking wedge, which means most space is created in the form of a graben above that wedge. Once the diapir starts piercing actively (figure 10b) the growth rate increases significantly, because (as is inherent in active piercement) the formation of accommodation space is no longer limited by the rate of extension. During this phase the growth rate accelerates as the overburden becomes thinner, until the diapir reaches the surface and the passive growth stage starts (figure 10c).

The diapir growth rates found for this model are not unlikely, as similar growth rates have been inferred for naturally occurring salt diapirs (e.g. growth rates of around 0.5 cm yr^{-1} up to almost 1 cm yr^{-1} have been inferred for the Sedom diapir in the Dead Sea basin (Weinberger et al. 2006).

4.2 Extension rate

The first parameter that will be assessed is the extension rate. While the velocity of salt flow is primarily influenced by the loading forces of the overburden, the flow can be inhibited by a lack of space to flow to. The extension rate directly influences the amount of space created.

The runs described below are the same as the reference model, with the exception of different extension rates; 0.02 cm.$year^{-1}$, 2 cm.$year^{-1}$ and 20 cm.$year^{-1}$ respectively.

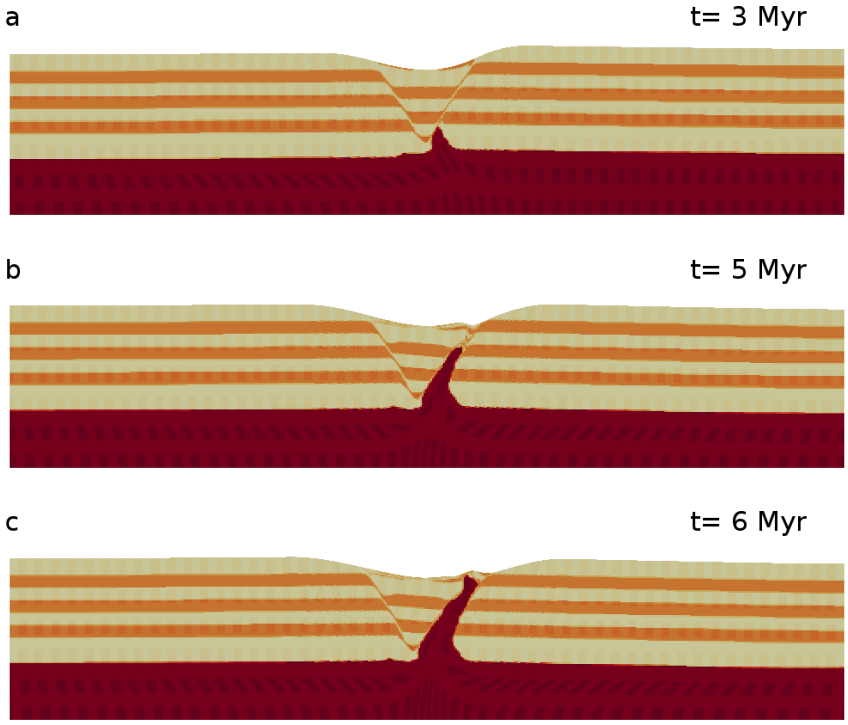

Figure 11: Evolution of a diapir in a system with an extension rate of 0.02 cm.$year^{-1}$. Note the far larger timespan than found for the reference model.

Figure 11 shows the results from the run with an extension rate of 0.02 cm.$year^{-1}$. The first noteworthy characteristic is the large timespan required for the diapir to reach the surface. Where the reference model reaches its final passive diapirism phase after approximately 1 Myr, this model only starts its active stage around 3 Myr and reaches the surface after a total of 6 Myr. The amount of space created by the extension is so minor that only a very small reactive diapir could be formed. However, the weakness of one of the faults alone is enough for the salt to find a way to actively push upwards, albeit very slowly.

The result of the run with an extension rate of 2 cm.$year^{-1}$ is shown in figure 12. It is clear that the timespan required for the diapir to reach the surface is now much smaller. In contrast

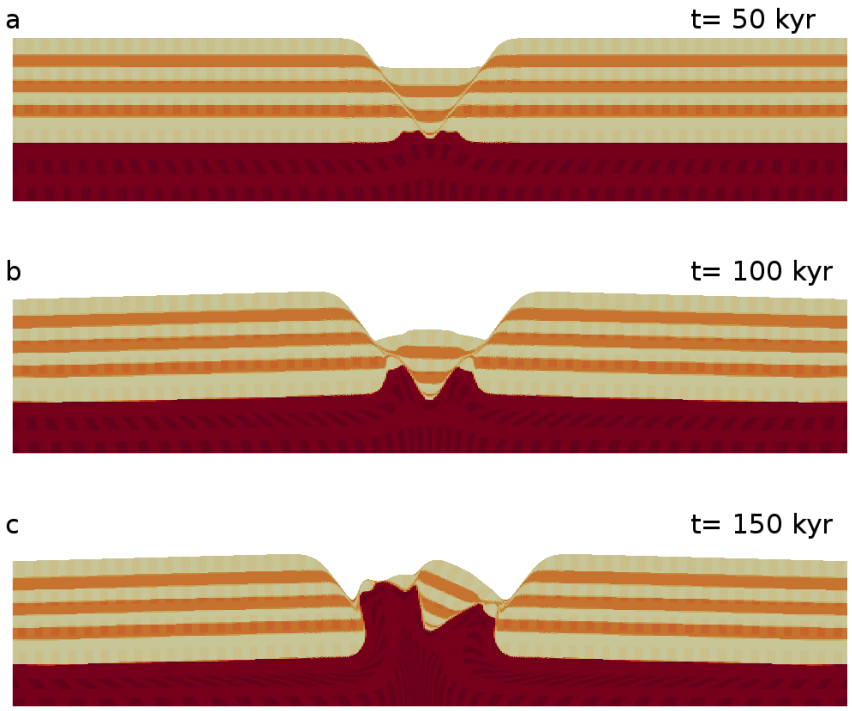

Figure 12: Evolution of a diapir in a system with an extension rate of 2 cm.year^{-1}. Note the broader shape than in the reference model.

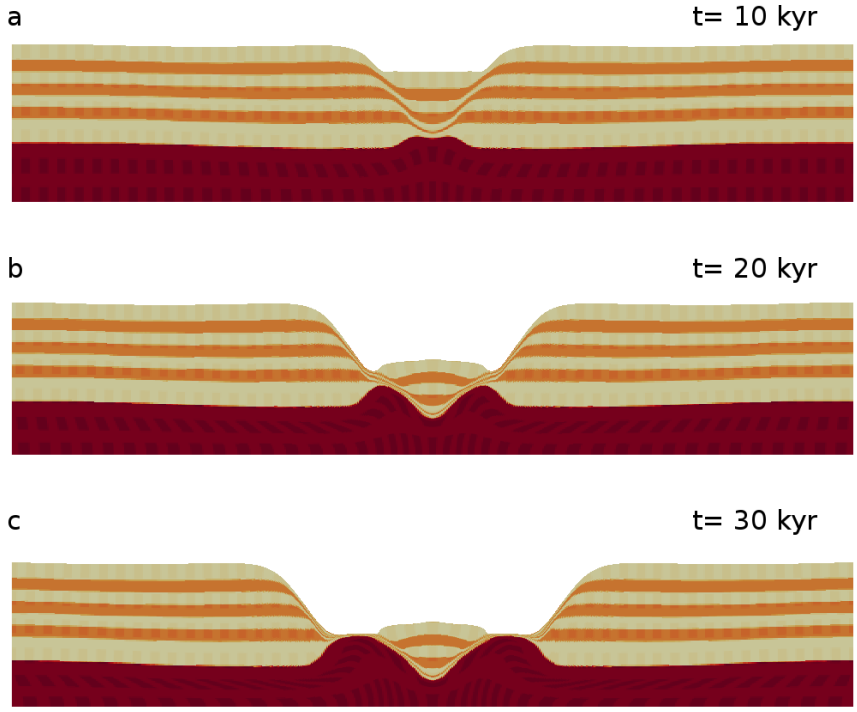

Figure 13: Evolution of a diapir in a system with an extension rate of 20 cm.year^{-1}. Note that the diapir(s) here do not advance beyond a pillow shape.

to the previous model, the reactive stage is again important. However, the numerical asymmetry which results in a "favoured" diapir during this stage seems to be less impactful, as both diapirs grow to almost the same size. Also the active piercement phase seems to be far more rigorous than in the reference model, because it pushes the wedge upwards almost to its original position. It also seems that the upwards growth rate of the diapir does not change as significantly as in the reference model, although it can be noted that the horizontal thickening of the diapir(s) advances further.

As seen in figure 13, a system put under an extension rate of 20 cm.year^{-1} does not advance beyond the reactional piercement stage, leaving only pillow shaped diapirs. The model evolves almost completely symmetrical. Besides the very short timespan in which this model evolves, there are not many noteworthy features. It should be noted that extension rates of this magnitude are geologically highly improbable.

It is clear that the rate of extension has a major impact on the shapes and growth rates of diapirs. Besides its direct influence on the total time required to evolve a diapir up to the surface, it also affects how long a system can remain in a reactive piercement stage.

Further testing with smaller domains, as well as with time-varying extension rates, has led to the understanding that whether or not the system is capable of advancing to an active piercement stage depends on both the extension rate and the buoyancy. Decreasing the domain size (and subsequently the buoyancy forces, as the material properties remain the same), decreases the threshold extension rate value above which the system remains in a reactive piercement stage. The factor in which the threshold rate decreases is almost 1-to-1 related to the factor in which the domain was decreased.

4.3 Surface processes

Next, the influence of rate of local erosion and deposition is looked at. As explained in section 3.3, a crude surface processes model was implemented that uses a diffusion type equation to simulate combined hill-slope processes (i.e. erosion of higher areas and deposition in lower areas). To change the rate of erosion and subsequent deposition, the mass diffusivity coefficient k_{sp} is varied. So in this case, the following two runs keep all parameters constant and at reference model values, but now $k_{sp} = 10^{-6}$ m^2.s^{-1} and $k_{sp} = 10^{-10}$ m^2.s^{-1} respectively.

Figure 14 shows the results of the first run ($k_{sp} = 10^{-6}$ m^2.s^{-1}). While the basin shoulders are uplifted slightly more than in the reference model due to the enhanced erosion, the wedge becomes heavier due to the sedimentation on top and is able to sink further into the salt than before. The improved sedimentation in the basin also keeps the overburden above the diapir somewhat thicker. This results in an overall lower diapir growth rate during its active stage than in the reference model, resulting in the diapir breaching the surface almost 500 kyr later. Another difference is that, where in the reference model the salt can at one point push the wedge slightly upwards, in this run, the wedge remains static during active diapirism. The final shape of this diapir is more cone-like, a result of more accomodation space at the base due to the longer timespan.

Figure 15 shows the results of the second run ($k_{sp} = 10^{-10}$ m^2.s^{-1}). Overall there are only a few differences between this run and the reference model. Less erosion of the basin shoulders allow for only slightly less uplift and the wedge remains somewhat smaller. Less sedimentation at the sides of the graben does however affect the thickness of the overburden above the diapir, resulting

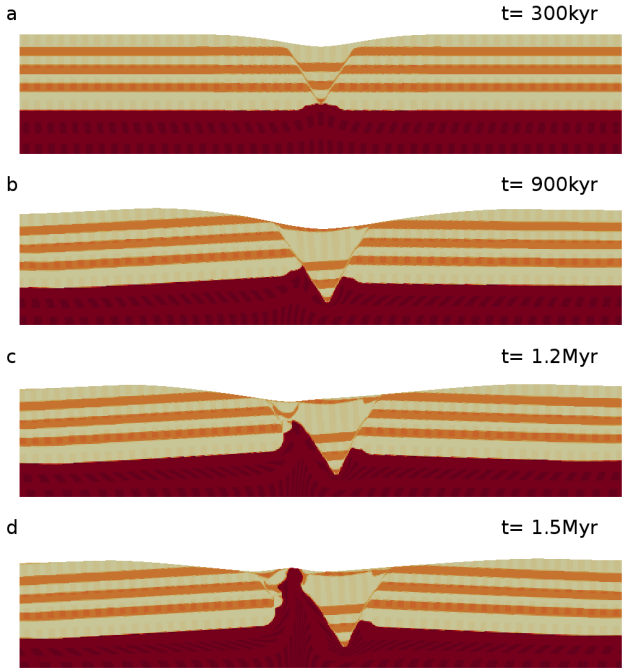

Figure 14: Evolution of a diapir in a system with an altered mass diffusivity constant of $k_{sp} = 10^{-6}$ m^2.s^{-1}.

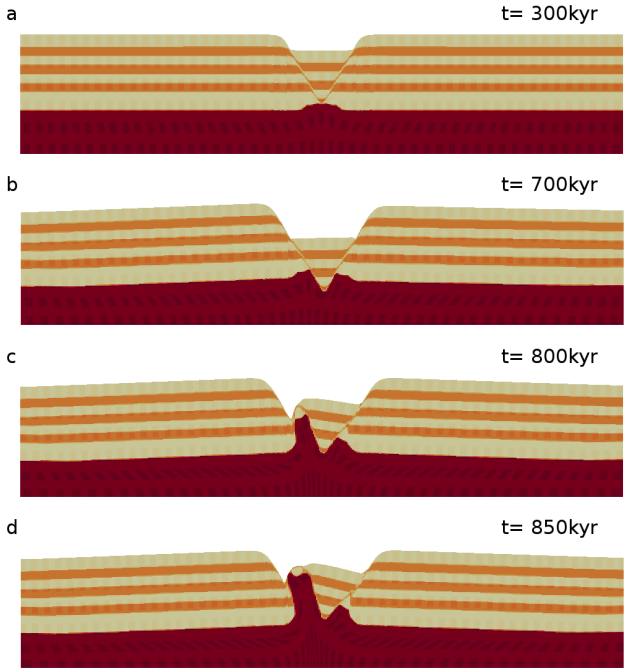

Figure 15: Evolution of a diapir in a system with an altered mass diffusivity constant of $k_{sp} = 10^{-10}$ m^2.s^{-1}.

in faster growth during active diapirism. The salt now reaches the surface after approximately 850 kyr. This faster growth over a shorter timespan results in an overall thinner diapir, with less difference in thickness between the base and the rest than the one in the reference model.

4.4 Density contrast

Naturally, the density contrast between the overburden and the salt is one of the most important factors that determine the buoyancy forces in the system. Although buoyancy is no longer seen as the primary control on diapirism, its effects must not be neglected. In the following runs the density of the overburden has been altered in order to increase or decrease the density contrast, which for the reference run was: $\rho_{salt}/\rho_{sed(mean)} = 2100/2450 = 0.86$. The first run now has a decreased mean density (ρ_{sed} =2155kg.m^3) of the sediments so that the density contrast is $\rho_{salt}/\rho_{sed} = 0.97$ and the second one has an increased ρ_{sed} of 2750kg.m^3, so that $\rho_{salt}/\rho_{sed} = 0.76$. Again all other parameters have reference model values. The results of both can be seen in figure 16.

The models start evolving absolutely identical until the wedge reaches the salt (at around 200 kyr, figure 16a). From this point onwards the lower contrast run (i.e. $\rho_{salt}/\rho_{sed} = 0.97$) evolves at a lower rate than the higher contrast run. It is clearly shown that during the active diapirism stage, the velocities reached by the salt in the latter are significantly higher (figure 16b and c as well as comparison to figure 10).

It can be concluded that the buoyancy forces in the system can significantly affect the growth rate of a diapir, although only during the active piercement phase. A higher density contrast leads to overall faster growth.

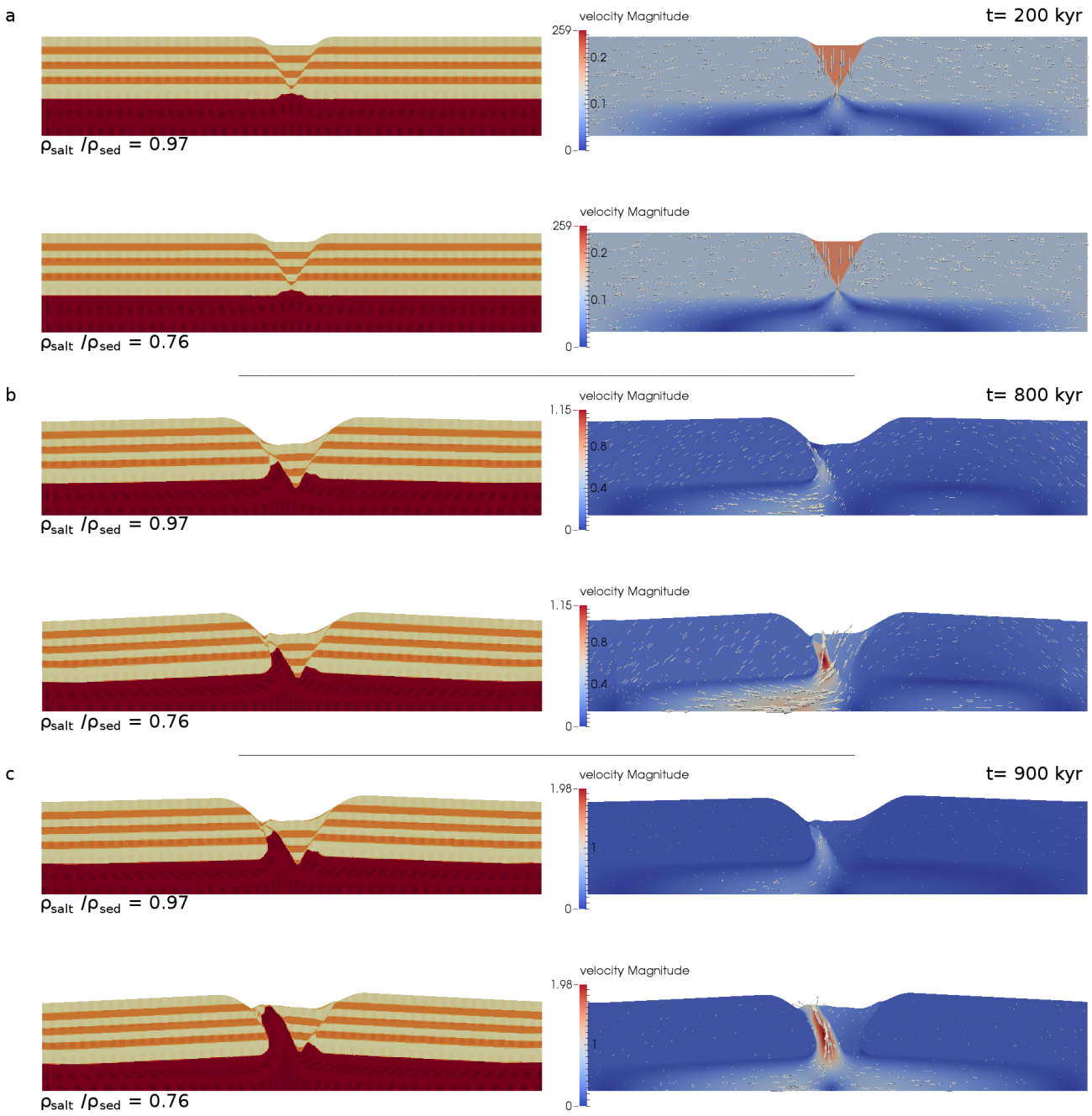

Figure 16: Results of the runs with different density contrasts. Velocities are in cm.year^{-1}.

4.5 Perturbed interfaces

All of the above models have a fully symmetrical setup, the asymmetry observed during the time evolution is a result of small numerical asymmetries in for example the surface processes algorithm. The following model starts off with an already slightly asymmetrical setup, in the form of some small (pseudo) random perturbations on each material interface. All other parameters are the same as for the reference model.

As can be seen in figure 17, the initial perturbations cause one of the set of conjugate faults

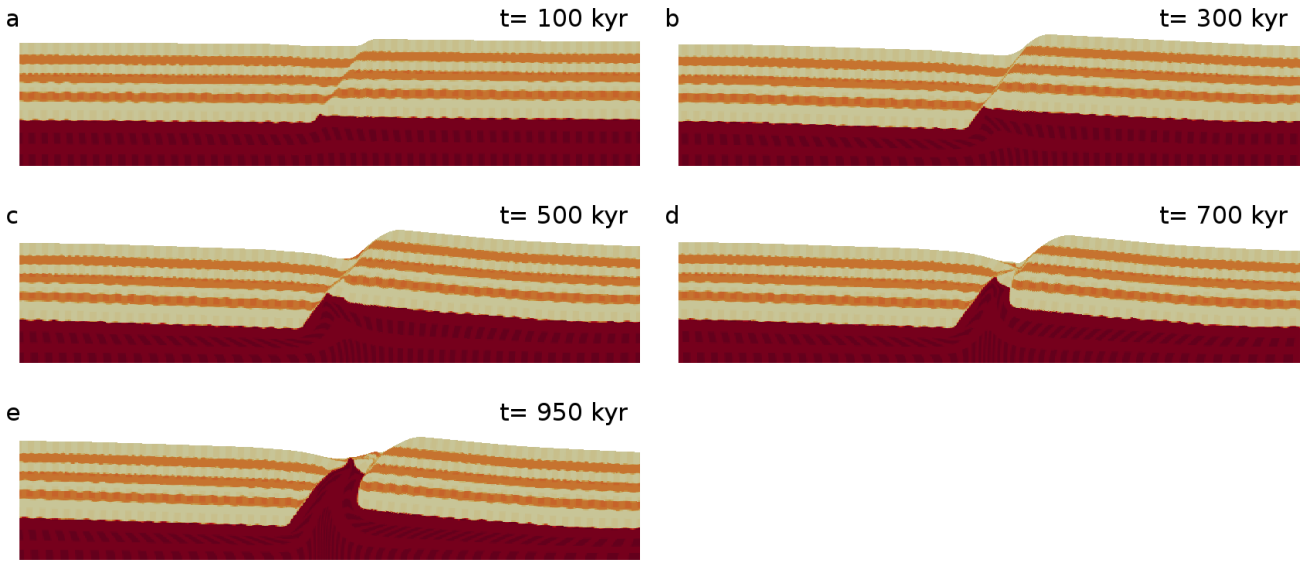

Figure 17: Evolution of a diapir in a system that starts of with perturbed material interfaces, making it more asymmetric. Note that the diapir(s) here do not advance beyond a pillow shape.

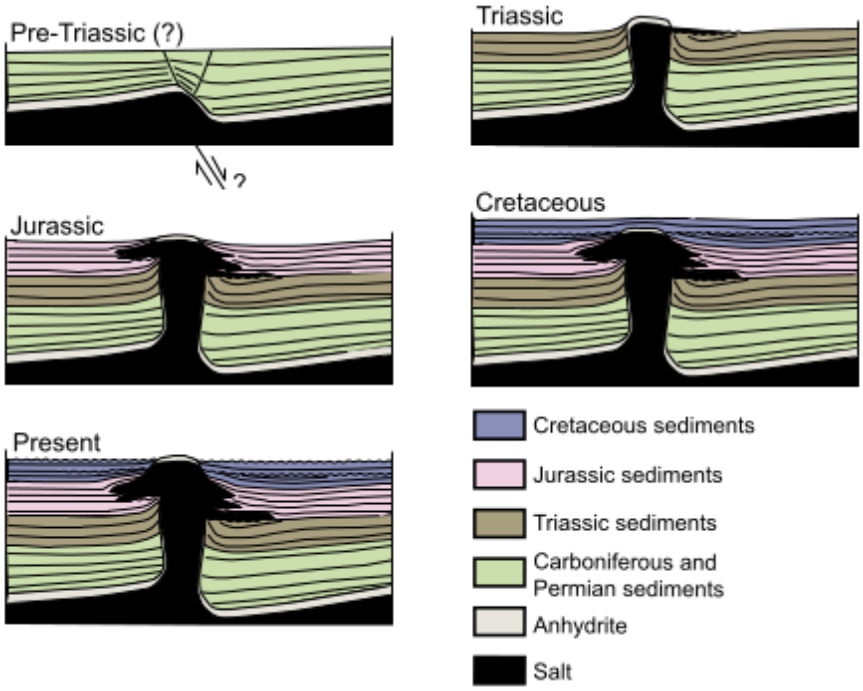

Figure 18: Schematic diagrams showing the development of the Hoodoo Dome on Ellef Ringes Island, Canadian Arctic Archipelago. Pre-Triassic to Triassic is similar to above model (figure 17). Altered from Boutelier et al. (2011).

to grow faster and ultimately accommodate all the extension. This causes a half-graben to form instead of the usual full graben. Although the resulting geometry is rather different, the timespan and duration of each stage of diapirism process remains mostly the same. Also during the

reactional phase, no real diapir is formed yet, as the salt moves mostly horizontal. Furthermore, diapir formation such as this has been seen as a possibility for naturally occurring diapirs, for example the Hoodoo Dome on Ellef Ringes Island, Canadian Arctic Archipelago (figure 18).

5 Temperature

The temperature evolution of a system is a feature that is almost impossible to asses in analogue models and even in most numerical studies to date (that deal with structural geological problems) the temperature field has only been instantaneously modelled. The next section regards the temperature evolution around a rising diapir during thin-skinned extension as before. Again a reference model is presented of which subsequently a parameter assessment is done.

5.1 Reference temperature model

Adding temperature to the models requires the addition of material thermal properties as well as temperature boundary conditions. To assess the impact of certain parameters, again a reference model is first created. The domain size, material layout, material properties and velocity boundary conditions are all identical to the reference model described in the previous section.

Added to the existing material properties is first off the internal heat production from radioactive decay H_r, which is set to 0 W.m^{-3} for all materials concerned. A negligible radiogenic heat production is considered realistic for most sedimentary rocks. Further thermal properties differ between the salt and the sedimentary rock types: the coefficient of thermal expansion α is set to 4.25 x 10^{-5} K^{-1} for the salt and to 3 x 10^{-5} K^{-1} for both sedimentary rocks, the heat capacity c_p is put at 518 J.kg^{-1}.K^{-1} for the salt and at 750 J.kg^{-1}.K^{-1} for the sediments. The thermal conductivity k of the salt has a value of 5.7 W.m^{-1}.K^{-1} and both sediments have a k of 2.25 W.m^{-1}.K^{-1}.

The thermal boundary conditions are as follows: the bottom boundary has a constant temperature of 473.15 K (200 ^{o}C), the top of the domain has a T of 273.15 K (0 ^{o}C). Furthermore the initial temperature gradient is assumed linear, which is quite realistic in the range of crust considered (Fowler 2005). Even so, initial testing has shown that within the first few timesteps, before any major tectonics occur, the temperature field reaches a steady state situation, where the gradient shows a kink on the salt-sediment interface (figure 19a).

The results of the reference model run are presented in figure 19. Even though the density is now temperature coupled, there is no noteworthy change in tectonics with respect to the reference model without temperature. This is not unexpected as we are dealing with geologically quite small temperature differences.

What is unexpected is how little the diapir disturbs the temperature field. Beneath its base, a noticeable decrease in temperature within the salt itself is seen and surrounding the rest of the rising salt body is a slight temperature increase of up to some 20 K, which is reverted to normal within a few hundred meter from the diapir. Subsequently, a diapir shaped salt body at rest, with a heightened temperature and the same rheological parameters was modelled. This showed that the time required for such diapir to cool down to a steady state temperature field with the same characteristics as seen in the reference model above, is only in the order of some thousands of years (figure 20). When comparing this cooling rate to the growth rates of the diapirs found in

this work, this shows that on the tectonic timescale the warmer salt almost instantly cools down to near 'normal' temperature values when moved upwards, i.e. the salt adjusts almost instantly to a thermal equilibrium. Note that the initial temperature field within the bottom salt layer is also not yet in a steady state situation(figure 20a). Basically, only the shape of the geotherm gets adjusted to comply with the thermal properties of the salt.

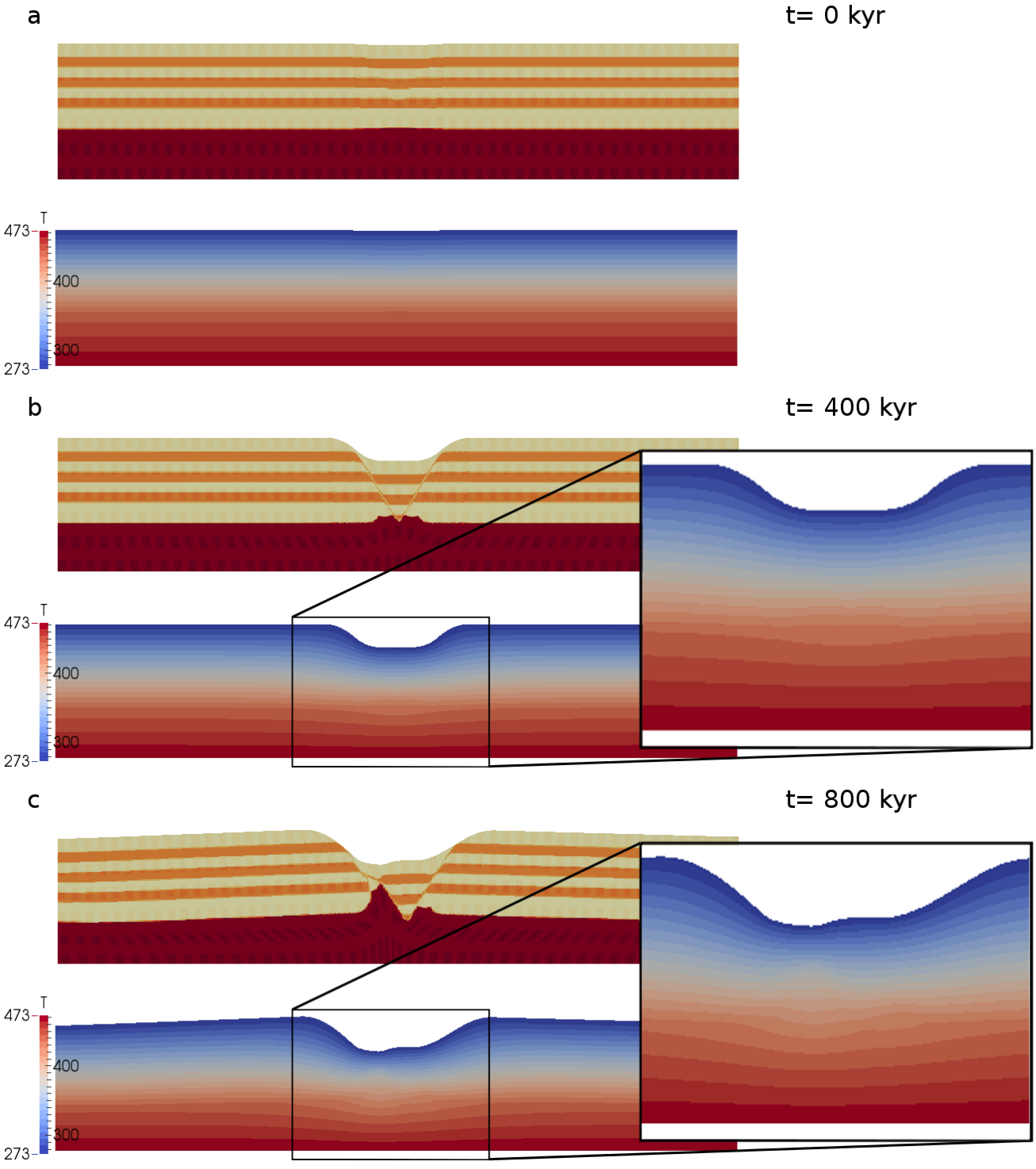

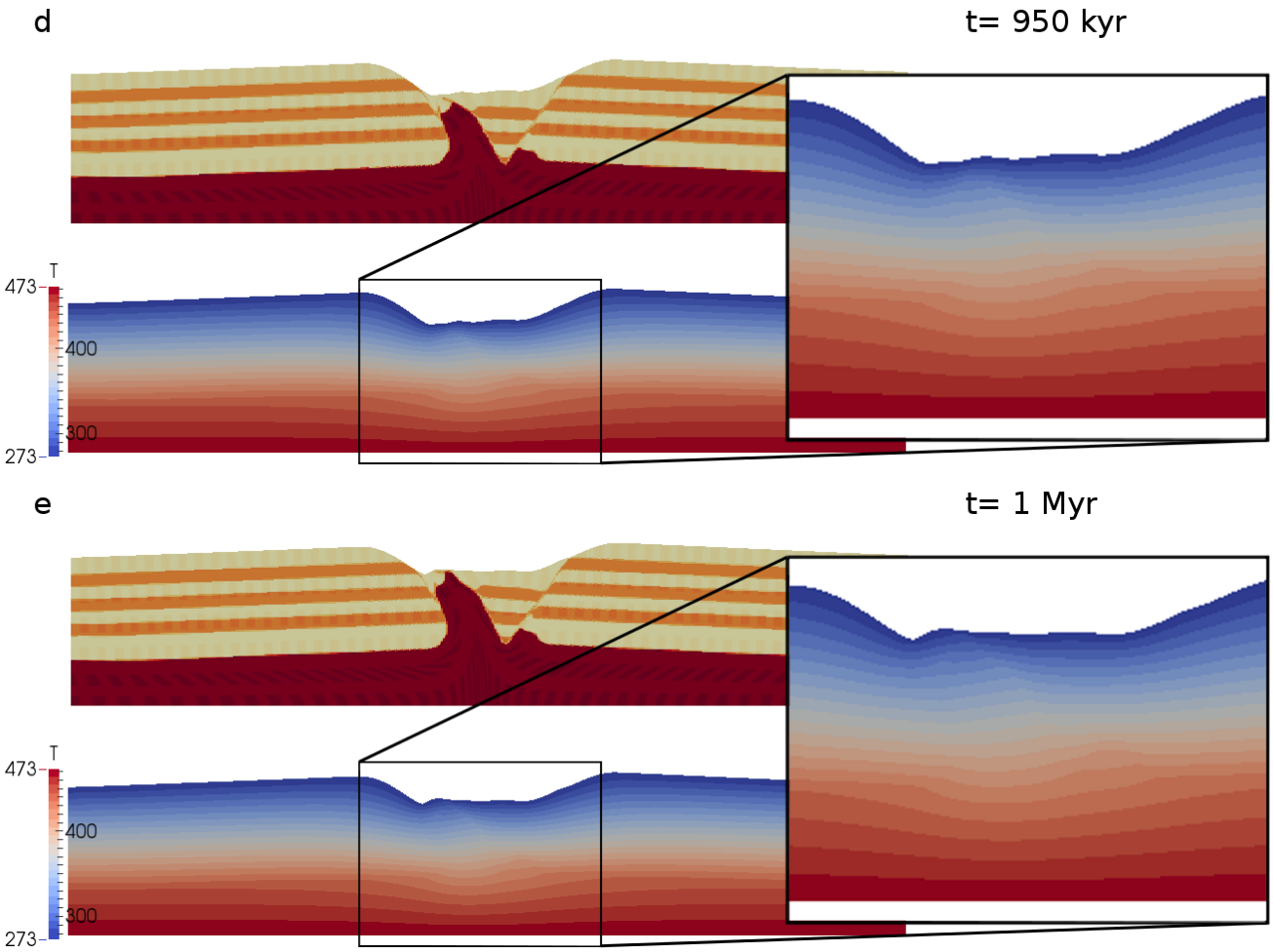

Figure 19: Temperature field evolution of the reference model.

A similar temperature field was gained from other numerical modelling experiments on diapirs by van Keken et al. (1993), although in their models all materials behave viscous and the full timespan of diapirism is significantly higher (figure 21).

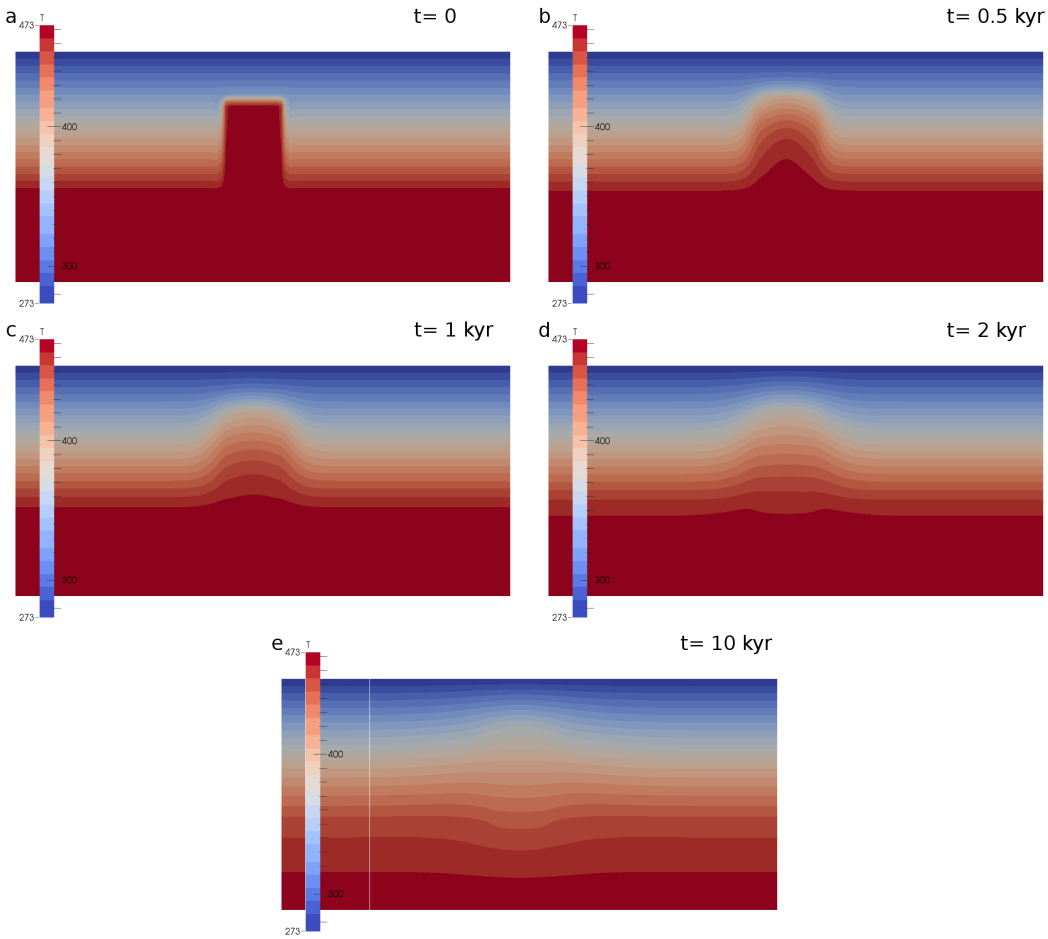

Figure 20: Temperature field evolution of a model with an increased bottom temperature of 573.15 K.

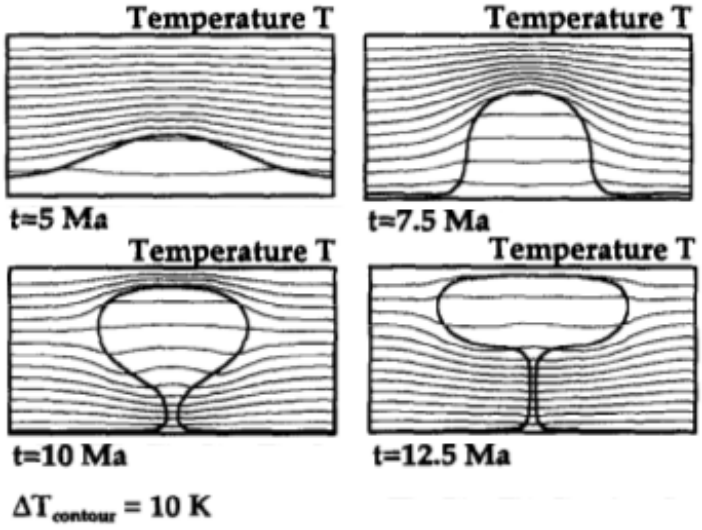

Figure 21: Time evolution of the temperature field in a diapirism model with all viscous rheologies. From van Keken et al. (1993)

5.2 Bottom temperature

The first parameter that will be assessed is the bottom temperature boundary value. While everything else remains identical to the reference model, the bottom temperature is now set to 573.15 K (300 ^{o}C). This will naturally increase the geothermal gradient in the system, although not much more is expected.

Figure 22 shows the results from this run. The only major change from the reference run is that the overall temperature gradient is indeed higher. Otherwise, the same factor of decrease and increase of temperature around the diapir is visible.

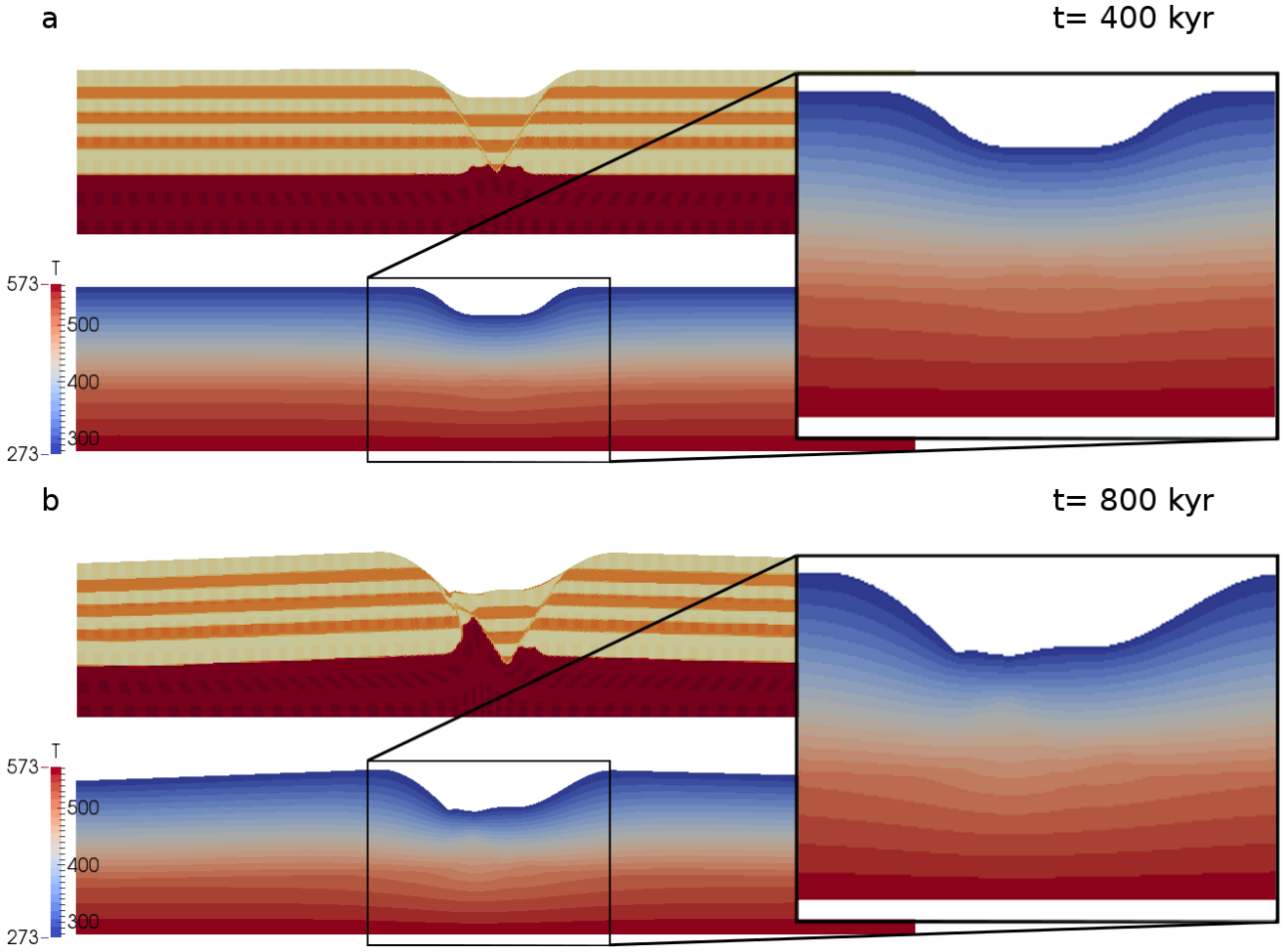

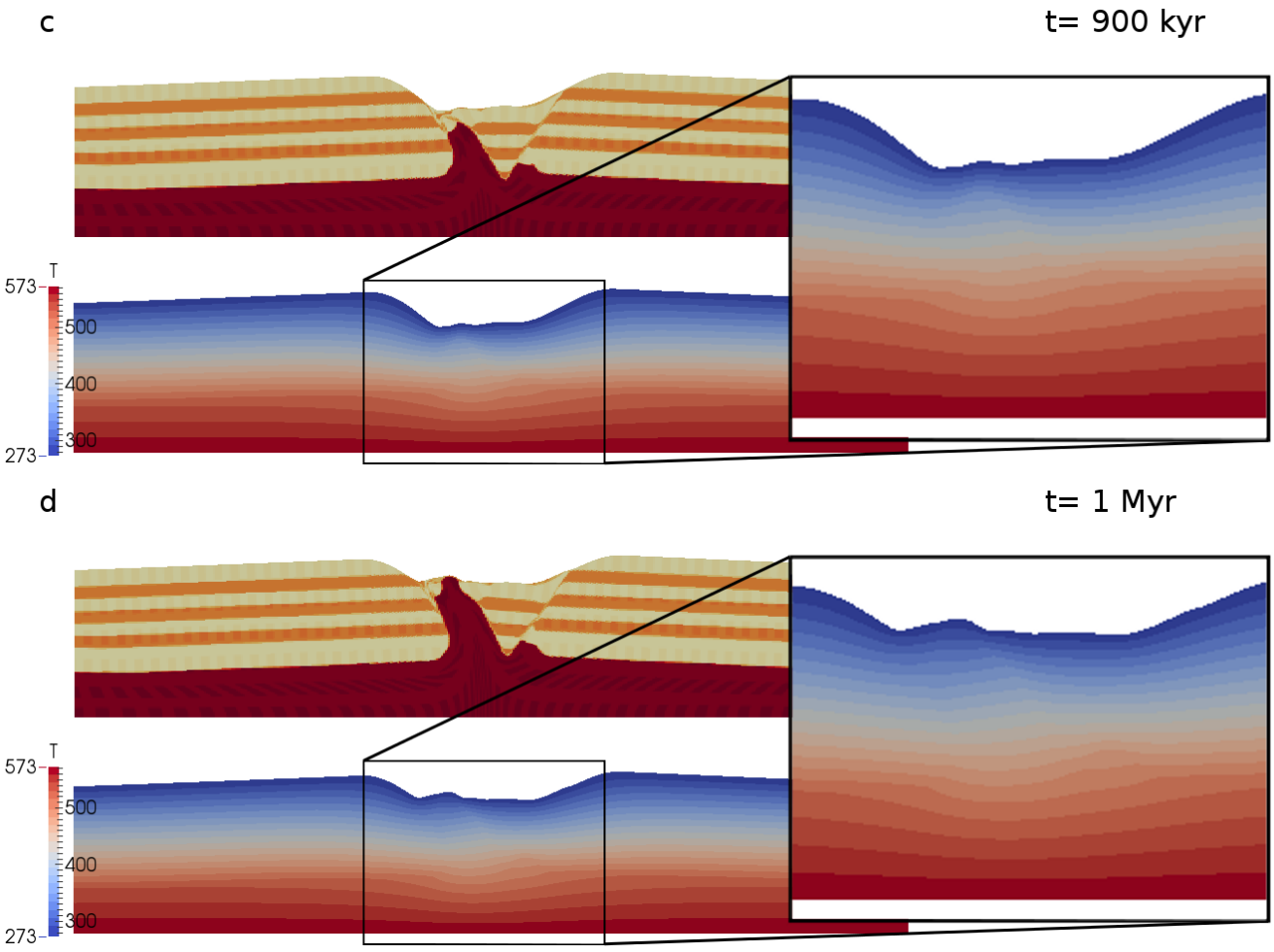

Figure 22: Temperature field evolution of a model with an increased bottom temperature of 573.15 K.

5.3 Salt conductivity

The second parameter that will be regarded, is the thermal conductivity k of the salt. Staying within realistic values for this temperature range, it is first lowered to 3 $W.m^{-1}.K^{-1}$. The second run uses a k of 6.1 $W.m^{-1}.K^{-1}$. All other parameters have reference values.

Comparing these two runs shows clear differences (figures 23 and 24). First of all, the initial thermal gradient in the salt layer with lower conductivity is less steep than the other, secondly almost zero effect on the temperature field around the diapir is seen in the former, while the latter shows it more clearly than the reference model.

6 Energy resources

In our society, the most important uses for the knowledge of the temperature field lie in the energy resource field, both hydrocarbon exploration and geothermal energy. For the former, the evolution of the temperature field is useful, whereas for the latter the present temperature field is important.

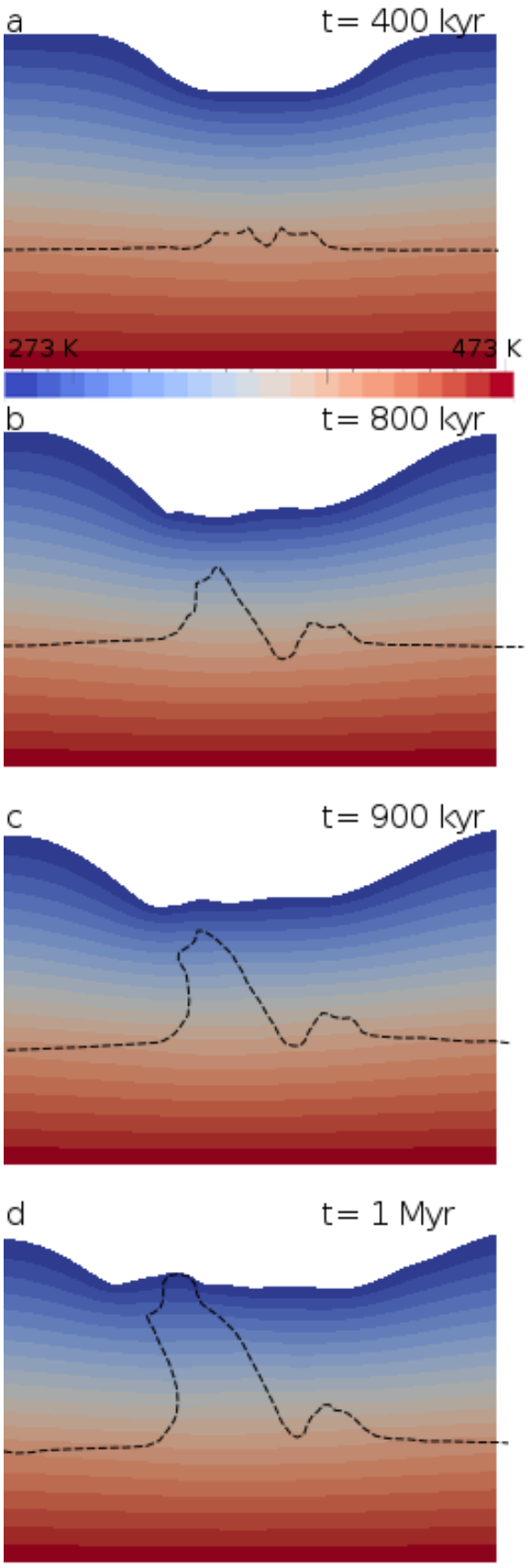

Figure 23: Temperature field evolution around a salt diapir with a conductivity of 3 $W.m^{-1}K^{-1}$. Dotted lines show the salt-sediment interface.

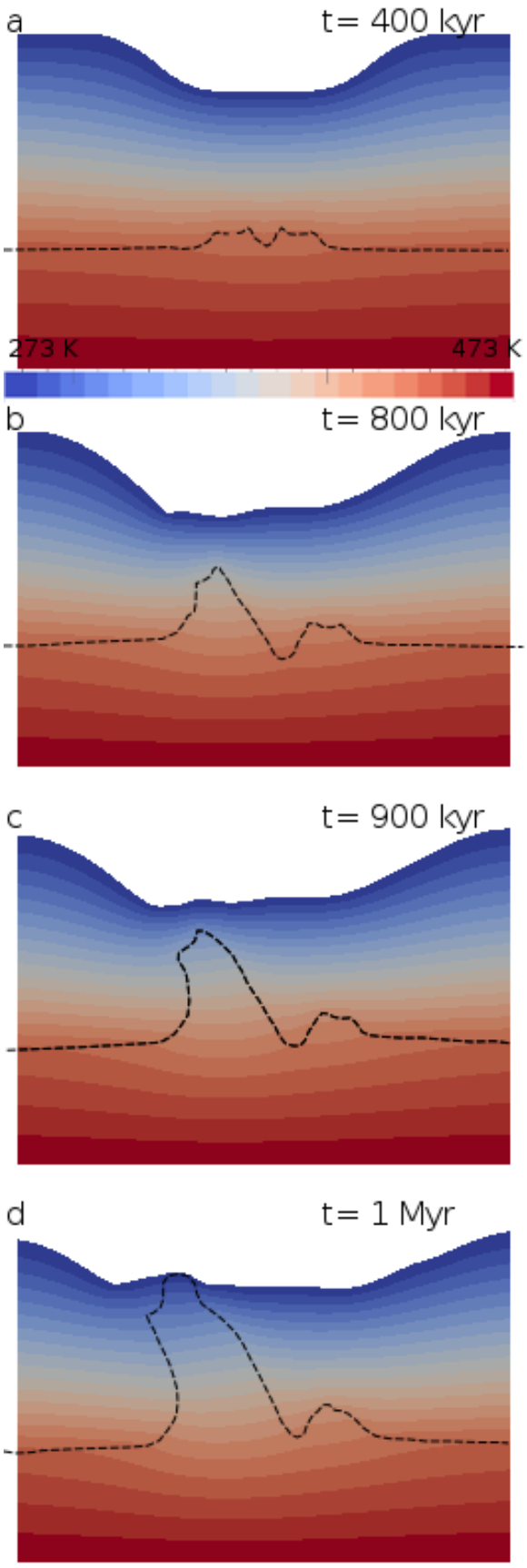

Figure 24: Temperature field evolution around a salt diapir with a conductivity of 6.1 $W.m^{-1}K^{-1}$. Dotted lines show the salt-sediment interface.

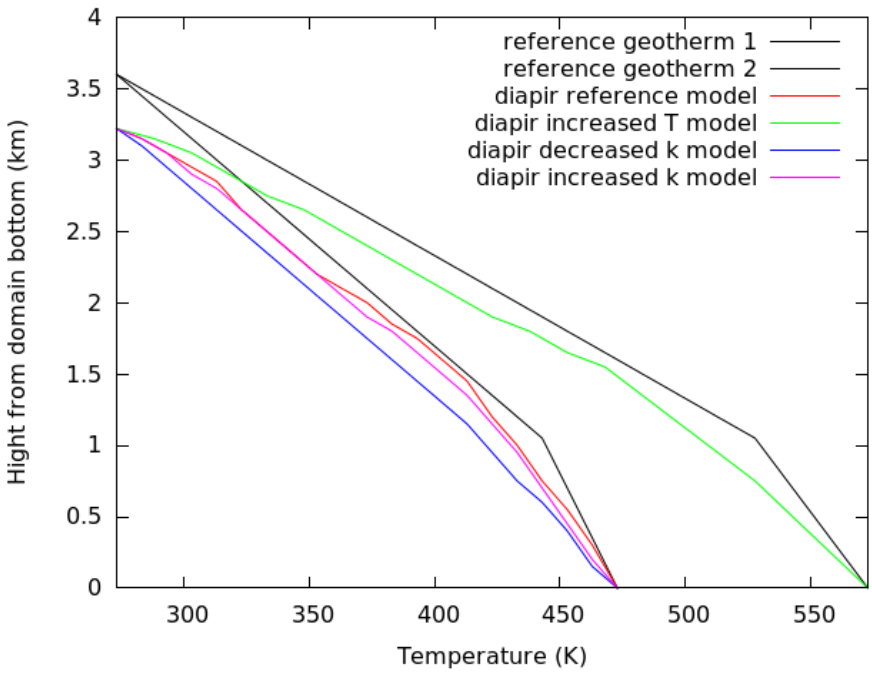

Figure 25: Thermal gradients through the diapirs of the previous models. In black are the two (for a bottom temperature of 473.15 K respectively 573.15 K) reference gradients taken away from the diapir.

Hydrocarbon source rocks only produce usable hydrocarbons during the time in which they are located within a certain temperature range, a so called maturation window (Kauerauf & Hantschel 2009). Under most circumstances the source rocks are being subjected to burial and subsequent temperature increase, whereby they go through a few stages of thermal maturity. Until approximately 60 ^{o}C the source rock remain immature. From $\approx$ 60 ^{o}C to $\approx$ 160 ^{o}C it is in its mature stage and produce most of its oil. Beyond $\approx$ 160 ^{o}C the rock is considered postmature for oil, but becomes mature for gas. In the case of above models, rocks located under normal circumstances above the 60 ^{o}C temperature line (above a depth of $\approx$ 800 m, or $\approx$ 500 m in the case of the heightened bottom temperature) but within a few hundred meters of the rising diapir might just shift over the maturity threshold, where they can remain for larger periods of time. The same goes for deeper source rocks, that may at one point in history have lain within the oil maturity field, until the diapir increased their temperatures above threshold values. Information on the current rise rate combined with knowledge of the rheologies and numerical models such as in this work, could determine how long ago the source rocks have started/stopped producing hydrocarbons, as well as give an indication of the size of these sources.

Thermal energy relies directly on the transfer of heat to the surface (Barbier 2002). This is either the natural heat flow through the Earths surface or withdrawal from depth, using for instance a water pumping system, where water is pumped down, gets heated up and returns to the surface with more energy than was used for the pump. The latter benefits just like the hydrocarbon exploration from heightened temperatures at depth. The former would benefit from locally increased surface heat flow. Figure 25 shows a few geothermal gradients obtained from

the model runs. As the local slope of a geotherm is a direct indication of the heat flux

$$q = k\left(\frac{dT}{dy}\right)$$

where k is the thermal conductivity, we can see that the heat flux at the top of the domain varies quite a bit for each run. The less steep a geotherm drops, the higher the heat flux. It is clear that in all cases the heat flux above the diapir is higher than away from the diapir. Both an increased bottom temperature and an increased salt conductivity give higher surface heat fluxes. During the rise of a diapir, the geotherm at that location changes shape continually. Comparing the depth and shape of a naturally occurring diapir to numerical models such as in this work can also give an indication of the surface heat flux, as well as the heat flux at depth.

7 Conclusions

Numerical modelling of diapirism during thin-skinned extension has provided some valuable insights.

Extension rates directly influence the total time required for the diapir to reach the surface, as well as how long the system remains in a state of reactional diapirism. With higher extension rates the diapir requires less time to reach the surface and remains in the reactional phase for a relatively longer period of time. The extension rate also affects the shape of the resulting diapir; higher extension rates cause an overall thicker diapir. The mass diffusivity coefficient, which determines how fast the surface gets reshaped, affects the thickness of the overburden in the graben. This subsequently affects the growth rate of the diapir during its active stage and the total rising time, which changes the shape of the diapir. A thicker overburden increases the total growth time and decreases the growth rate during active piercement. This enhances the cone shape of the diapir. The density contrast between the salt and the sediments also influences, through the buoyancy forces, the growth rate during active piercement. If random perturbations on the material interfaces become too large, the system can evolve even more asymmetrical, forming a half-graben instead.

Surrounding a rising diapir the temperature is heightened, although not as much as expected. This is due to the fact that the salt cools down significantly fast, so that it remains in thermal equilibrium with the surroundings. The salt emplaced within the sedimentary sequence therefore has only a slightly higher temperature, to a maximum of $\approx$ 20 K increase. Also, a higher conductivity gives a larger increase. Still, the resulting temperature increase of the surrounding rocks could be enough for a small reservoir of hydrocarbon source rock to achieve maturity. Combined with other data, this can be used to assess the duration in which a source rock has been producing hydrocarbons. The heat flux above the diapir is higher than away from the diapir. Besides, both an increased bottom temperature and an increased salt conductivity add to higher surface heat fluxes. Both a higher surface heat flux and a increased temperatures at depth can prove advantageous for geothermal energy production.

There are a few more concepts important to the modelling of diapirism during thin-skinned extension. First of all the effect of adding a third dimension to the models could lead to better constrained effects of each parameter. Secondly a few of the parameters were still temperature independent, which is not always realistic (see figure 3). A third factor that was neglected in

this study is possible larger distance mass transport, i.e sedimentation without the need for local erosion as well as the other way around. Another feature that is not yet assessed is the possibility that the whole sequence is slightly tilted as in a passive margin situation. Overall there is still room for much more research on this topic.

Acknowledgements

I would like to thank dr. Cedric Thieulot for his valuable insights and guidance and for providing the code that made this research possible. I also wish to thank both prof. dr. Wim Spakman for his part in helping me set up this master research and dr. Damien Bonté for his help in the formation of the research subject.

References

Anderson, J. 1995, Computational Fluid Dynamics

Barbier, E. 2002, Geothermal energy technology and current status: an overview, Renewable and Sustainable Energy Reviews, 188, 3

Blesh, C. J., Kulacki, F. A., & Christensen, R. N. 1983, Application of integral methods to prediction of heat transfer from a nuclear waste repository., Open file report ONWI-495, 12

Boutelier, J., Cruden, A., Brent, T., & Stephenson, R. 2011, Timing and mechanisms controlling evaporite diapirism on Ellef Ringnes Island, Canadian Arctic Archipelago, Basin Research, 23, 478âĂŞ498

Brun, J. P. & Fort, X. 2008, Entre sel et terre

Brun, J. P. & Fort, X. 2011, Salt tectonics at passive margins: Geology versus models, Marine and Petroleum Geology, 28, 1123

Brun, J. P. & Mauduit, T. P. O. 2009, Salt rollers: Structure and kinematics from analogue modelling, Marine and Petroleum Geology, 26, 249

Carter, N. L., Horseman, S. T., Russell, J. E., & Handin, J. 1993, Rheology of rocksalt, Journal of Structural Geology, 15, 1257

Fowler, C. M. R. 2005, The Solid Earth - an introduction to global geophysics

Fuchs, L., Koyi, H., & Schmeling, H. 2015, Numerical modeling of the effect of composite rheology on internal deformation in down-built diapirs, Tectonophysics, 646, 79âĂŞ95

Harding, R. & Huuse, M. 2015, Salt on the move: Multi stage evolution of salt diapirs in the Netherlands North Sea, Marine and Petroleum Geology, 61, 39

Harms, G. L. 2015, Guided research: Finite Element Method coding, towards salt tectonics research

Hartz, E. H. & Podladchikov, Y. Y. 2008, Toasting the jelly sandwich: The effect of shear heating on lithospheric geotherms and strength, Geology, 36, 331

Hudec, M. R. & Jackson, M. P. A. 2007, Terra infirma: Understanding salt tectonics, Earth-Science Reviews, 82, 1

Jackson, M. P. A. & Talbot, C. J. 1986, External shapes, strain rates, and dynamics of salt structures, Geological Society of America Bulletin, 97, 305

Kachanov, L. M. 2004, Fundamentals of the Theory of Plasticity

Kauerauf, A. I. & Hantschel, T. 2009, Fundamentals of Basin and Petroleum Systems Modeling

Kittenrød, I. H. 2011, PhD thesis, Department of Geoscience, University of Bergen, Norway

Massimi, P., Quarteroni, A., Saleri, F., & Scrofani, G. 2007, Modeling of salt tectonics, Comput. Methods Appl. Mech. Engrg., 197, 281âĂŞ293

Nalpas, T. & Brun, J. P. 1993, Salt flow and diapirism related to extension at crustal scale, Tectonophysics, 228, 349

Nikolinakou, M. K., Flemings, P. B., & Hudec, M. R. 2013, Modeling stress evolution around a rising salt diapir, Marine and Petroleum Geology, 51, 230

Petersen, K. & Lerche, I. 1994, quantification of thermal anomalies in sediments around salt structures, Geothermics, 24, 253

Podladchikov, Y., Talbot, C., & Poliakov, A. N. B. 1993, Numerical models of complex diapirs, Tectonophysics, 228, 189

Poliakov, A. N. B., Podladchikov, Y., & Talbot, C. 1993, Initiation of salt diapirs with frictional overburdens: numerical experiments, Tectonophysics, 228, 199

Schott, B., Yuen, D. A., & Schmeling, H. 2000, The significance of shear heating in continental delamination, Physics of the Earth and Planetary Interiors, 118, 273

Schultz-Ela, D. D. & Walsh, P. 2002, Modeling of grabens extending above evaporites in Canyonlands National Park, Utah, Journal of Structural Geology, 24, 247

Spiers, C. J., Schutjens, P. M. T. M., Brzesowsky, R. H., et al. 1990, Experimental determination of constitutive parameters governing creep of rocksalt by pressure solution, Geological Society Special Publication, 54, 215

Thielmann, M. & Kaus, B. J. P. 2012, Shear heating induced lithospheric-scale localization: Does it result in subduction?, Earth and Planetary Science Letters, 359-360, 1

Thieulot, C. 2011, FANTOM: Two- and three-dimensional numerical modelling of creeping flows for the solution of geological problems, Physics of the Earth and Planetary Interiors, 188, 47

Thieulot, C. 2014, ELEFANT: a user-friendly multipurpose geodynamics code, subm. to Solid Earth

van Keken, P. E., Spiers, C. J., van den Berg, A. P., & Muyzert, E. J. 1993, The effective viscosity of rocksalt: implementation of steady-state creep laws in numerical models of salt diapirism, Tectonophysics, 225, 457

Vendeville, B. C. & Jackson, M. P. A. 1992, The rise of diapirs during thin-skinned extension, Marine and Petroleum Geology, 9, 331

Weinberger, R., Begin, Z. B., Waldmann, N., et al. 2006, Quaternary rise of the Sedom diapir, Dead Sea basin, Geological Society of America Special Publication, 401, 33

Zaleski, S. & Julien, P. 1992, Numerical simulation of Rayleigh-Taylor instability for single and multiple salt diapirs, Tectonophysics, 206, 55

Appendix A

run	ext. rate (cm.year^{-1})	k_{sp} (m^2.s^{-1})	$\rho_{salt}/\rho_{sed(mean)}$	interface perturb.	bottom T (K)	k (W.m^{-1}K^{-1})	fig.
reference	0.2	10^{-8}	0.86	no	-	-	7
ext. rate 1	0.02	10^{-8}	0.86	no	-	-	9
ext. rate 2	2.0	10^{-8}	0.86	no	-	-	10
ext. rate 3	20.0	10^{-8}	0.86	no	-	-	11
surf p. 1	0.2	10^{-6}	0.86	no	-	-	12
surf p. 2	0.2	10^{-10}	0.86	no	-	-	13
dens 1	0.2	10^{-8}	0.97	no	-	-	14
dens 2	0.2	10^{-8}	0.76	no	-	-	14
perturb.	0.2	10^{-8}	0.86	yes	-	-	15
temp ref	0.2	10^{-8}	0.86	no	473.15	5.7	16
temp bottom T	0.2	10^{-8}	0.86	no	573.15	5.7	17
temp cond. 1	0.2	10^{-8}	0.86	no	473.15	6.1	18
temp cond. 2	0.2	10^{-8}	0.86	no	473.15	3.0	19

Table 1: Overview of adjusted parameters of the model runs shown in this work.